2019

Insight of a Phase Compatible Surface Coating for Long-Durable Li-Rich Layered Oxide Cathode

Sijiang Hu
Huanggang Normal University, University of Wollongong, sijiang@uow.edu.au

Yu Li
Guangxi Normal University

Yuhua Chen
Guangxi Normal University

Jiming Peng
Huanggang Normal University, Guangxi Normal University

Tengfei Zhou
University of Wollongong, tengfeiz@uow.edu.au

See next page for additional authors

Publication Details

Hu, S., Li, Y., Chen, Y., Peng, J., Zhou, T., Pang, W., Didier, C., Peterson, V. K., Wang, H., Li, Q. & Guo, Z. (2019). Insight of a Phase Compatible Surface Coating for Long-Durable Li-Rich Layered Oxide Cathode. Advanced Energy Materials, 9 (34), 1901795-1-1901795-10.

Insight of a Phase Compatible Surface Coating for Long-Durable Li-Rich Layered Oxide Cathode

Abstract

Li-rich layered oxides (LLOs) can deliver almost double the capacity of conventional electrode materials such as LiCoO2 and LiMn2O4; however, voltage fade and capacity degradation are major obstacles to the practical implementation of LLOs in high-energy lithium-ion batteries. Herein, hexagonal La0.8Sr0.2MnO3−y (LSM) is used as a protective and phase-compatible surface layer to stabilize the Li-rich layered Li1.2Ni0.13Co0.13Mn0.54O2 (LM) cathode material. The LSM is Mn□O□Mbonded at the LSM/LM interface and functions by preventing the migration of metal ions in the LM associated with capacity degradation as well as enhancing the electrical transfer and ionic conductivity at the interface. The LSM-coated LM delivers an enhanced reversible capacity of 202 mAh g−1at 1 C (260 mA g−1) with excellent cycling stability and rate capability (94% capacity retention after 200 cycles and 144 mAh g−1 at 5 C). This work demonstrates that interfacial bonding between coating and bulk material is a successful strategy for the modification of LLO electrodes for the next-generation of high-energy Li-ion batteries.

Disciplines

Engineering | Physical Sciences and Mathematics

Publication Details

Hu, S., Li, Y., Chen, Y., Peng, J., Zhou, T., Pang, W., Didier, C., Peterson, V. K., Wang, H., Li, Q. & Guo, Z. (2019). Insight of a Phase Compatible Surface Coating for Long-Durable Li-Rich Layered Oxide Cathode. Advanced Energy Materials, 9 (34), 1901795-1-1901795-10.

Authors

Sijiang Hu, Yu Li, Yuhua Chen, Jiming Peng, Tengfei Zhou, Wei Kong Pang, Christophe R. Didier, Vanessa K. Peterson, Hongqiang Wang, Qingyu Li, and Zaiping Guo

Insight of A Phase Compatible Surface-Coating for Long-Durable Li-rich Layered Oxide Cathode

Sijiang Hu, Yu Li, Yuhua Chen, Jiming Peng, Tengfei Zhou, Wei Kong Pang,* Christophe Didier, Vanessa K. Peterson, Hongqiang Wang,* Qingyu Li, and Zaiping Guo*

Dr. S. J. Hu, J. M. Peng, Prof. H. Q. Wang

Hubei Key Laboratory for Processing and Application of Catalytic Materials, College of Chemistry and Chemical Engineering,

Huanggang Normal University, Huanggang 438000, P.R. China

E-mail: whq74@126.com

Dr. S. J. Hu, Dr. T. F. Zhou, Dr. W. K. Pang, Dr. C. Didier, Prof. V. K. Peterson, Prof. Z. P. Guo

Institute for Superconducting and Electronic Materials, School of Mechanical, Materials, Mechatronic, and Bio-medical Engineering,

University of Wollongong, NSW 2500, Australia

E-mail: wkpang@uow.edu.au; zguo@uow.edu.au

Y. Li, Y. H. Chen, J. M. Peng, Prof. H. Q. Wang, Prof. Q. Y. Li
Guangxi Key Laboratory of Low Carbon Energy Materials, School of Chemistry and Pharmaceutical Sciences,

Guangxi Normal University, Guilin 541004, P.R. China

Dr. C. Didier, Prof. V. K. Peterson

Australian Centre for Neutron Scattering, Australian Nuclear Science and Technology Organization, Locked Bag 2001, Kirrawee DC, New South Wales 2232, Australia

Keywords: lithium-ion batteries; Li-rich layered oxide; surface-coating; voltage fade; metal ion migration

Abstract: Li-rich layered oxides (LLOs) can deliver almost double the capacity of conventional electrode materials such as $LiCoO_2$ and $LiMn_2O_4$, however, voltage fade and capacity degradation are major obstacles to the practical implementation of LLOs in high-energy lithium-ion batteries. Herein, hexagonal $La_{0.8}Sr_{0.2}MnO_{3-y}$ (LSM) is used as a protective and phase-compatible surface layer to stabilize the Li-rich layered $Li_{1.2}Ni_{0.13}Co_{0.13}Mn_{0.54}O_2$ (LM) cathode material. The LSM is Mn-O-*M* bonded at the LSM/LM interface and functions by preventing the migration of metal ions in the LM associated with capacity degradation as well as enhancing the electrical transfer and ionic conductivity at the interface. The LSM-coated LM delivers an enhanced reversible capacity of 202 mAh g^{-1} at 1 C (260 mA g^{-1}) with excellent cycling stability and rate capability (94% capacity retention after 200 cycles and 144 mAh g^{-1} at 5 C). This work demonstrates that interfacial bonding between coating and bulk material is a successful strategy for the modification of LLO electrodes for the next-generation of high-energy Li-ion batteries.

1. Introduction

Since their commercialization less than 30 years ago, lithium-ion batteries (LIBs) have experienced significant development and are used in electrified vehicle (EV) applications among various other technologies. The International Energy Agency reports that the number of EVs, including plug-in hybrid electric vehicles, surpassed 3 million in 2017 (Global EV Outlook 2018: towards cross-modal electrification. International Energy Agency, Paris 2018), which is a 56% increase from 2016, and that the main performance features of LIB powered EVs (safety, range, and cost) are approaching to that of gasoline vehicles. For example, the Tesla Model 3 (https://www.tesla.com/model3) has a driving range of up to 310 miles on a single charge and can charge to ~ 60% full in 15 minutes, with a charge cost of approximately $0.26 per kilowatt hour. To meet the increasing demands of the EV market, LIB energy/power density, cycle life, and fast charging capability must be improved, with the cathode material of LIBs being the bottleneck in meeting these challenges. Several commercialized materials, such as $LiCoO_2$, $LiMO_2$ (M = Ni, Co, Mn, etc.), $LiMn_2O_4$, and $LiFePO_4$, are unable to fully satisfy the growing demand for high energy density batteries. Layered Li-rich oxide materials such as $Li_{1+x}Mn_{1-x-y}M_yO_2$ ($0 < x+y < 1$, *M* = transition metal) have been studied intensively with the aim of achieving a capacity beyond 250 mAh g^{-1} and an energy density beyond 900 Wh kg^{-1}.[1] Unfortunately, significant

challenges including a large first-cycle irreversible capacity loss, unsatisfactory cycle performance, and rate capability issues, need to be overcome before these materials can be advanced to practical application.[2] Notably, these materials suffer voltage fade during electrochemical cycling, resulting from a layered-spinel transition,[3] unfavorable redox couple evolution during cycling,[4] and the formation of partial dislocations.[5] Efforts to overcome these specific problems have been focused on the $Li_{1.2}Ni_{0.13}Co_{0.13}Mn_{0.54}O_2$ material as a result of its particularly high specific capacity and good cyclability.[6-7] The strategies employed to improve the performance of LLOs can be broadly classified into three groups: particle size control,[8] lattice doping,[9-10] and surface modification.[11-12] Although nanosizing has been successfully used to increase the capacity and rate performance of LLOs,[13] the resulting increased surface energy and area of the material along with decreased density lead to agglomeration of the material as well as severe side reaction with the electrolyte.[14] Dopants have also been introduced successfully to stabilize the LLO structure,[15] however, the atomic-scale engineering of such doping is challenging.[16] Although compositional changes in electrodes during electrochemical processes are leading factors of cycle instability,[17-18] the electrode surface may compositionally differ to that of the bulk particle, and surface coatings and other modifications have been successfully employed to protect against electrode degradation without changing the bulk electrode structure, particularly for high-voltage electrode materials. To date, coatings applied to LLO to improve their stability include Al_2O_3,[19] SnO_2,[20] TiO_2,[21] AlF_3,[22] Li_2SiO_3,[23] Li_3PO_4,[24] Li_2ZrO_3,[25] and $LiVO_3$.[26]

Typically, surface modification offers either a better electronic conductivity and hinders lithium diffusion, or provides fast ion conduction and blocks electron transportation. Double-layer coatings have been proposed as an approach to promote both electronic and ion conduction.[27,28] The hybrid Mg^{2+} and Li-Mg-PO_4 layer was successfully used to improve cycle stability of the $Li_{1.17}Ni_{0.17}Co_{0.17}Mn_{0.5}O_2$ material[29] by inhibiting undesired reactions such as attack by the HF generated during electrolyte decomposition at high voltage and subsequent migration of atoms from the M layer, however, it did

not significantly enhance both electronic and ionic conductivity. Whilst promising, the compatibility of the coating and electrode materials can be an issue for long-term cycling. Perovskite-type $La_{1-x}Sr_xMnO_{3-y}$, with $R\bar{3}c$ space group symmetry is a high stability solid oxide fuel cell cathode with a high concentration of oxygen vacancies leading to good electronic conductivity.[30-31] Importantly, this material has been used as a coating to suppress Mn dissolution from and enhance the electronic conductivity of both $LiNi_{0.5}Mn_{1.5}O_4$ and $LiMn_2O_4$ electrode materials.[32-33] The high oxygen vacancy content of $La_{1-x}Sr_xMnO_{3-y}$ may also play a role in reducing the oxygen loss occurring at the surface of high-voltage electrodes, which is detrimental to battery performance.[31,34-35] Herein, we introduce $La_{0.8}Sr_{0.2}MnO_{3-y}$ (LSM) as a coating on the $Li_{1.2}Ni_{0.13}Co_{0.13}Mn_{0.54}O_2$ (LM) electrode material, building on our previous work investigating LSM,[36] and reveal in detail its mechanism for the performance enhancement of LM.

2. Results and discussion

As-prepared pristine LM and LSM-coated LM with coatings of 0.5, 1.0, 2.0, and 3.0 wt.% LSM (denoted LSM0.5, LSM1, LSM2, and LSM3, respectively) were characterized using X-ray powder diffraction (XRPD) (Figure. S1). Neutron powder diffraction (NPD) data of LM and LSM2 were also collected and analyzed using the Rietveld method, with the refined profiles shown in Figure 1a-b and the obtained crystallographic details given in Table S1. Both LM and LSM2 are found to be a two-phase composite system as consistent with that for the LM material,[15] consisting of a hexagonal LiMO$_2$ phase with space group $R\bar{3}m$ (JCPDS entry 52-0457) and a monoclinic Li_2MnO_3 phase with space group $C2m$ (JCPDS entry 27-1252)[37] with a Li_2MnO_3 weight fraction of 6.7(4) and 5.9(4) wt.%, respectively. LiMO$_2$ in LM and LSM2 have similar lattice parameters, with the LSM coating inducing a ~ 0.014(1)% expansion in the *c* parameter compared to the pristine material, indicating no significant impact of the coating on the LM unit cell. Given that the ionic radii of La^{3+} and Sr^{2+} (11.7 and 11.8 Å, respectively) are much larger than *M* in LiMO$_2$, the incorporation of these large ions into the crystal structure of LM as dopants is unlikely. When the coating is increased to 3.0 wt.%, weak reflections arising from $La_{0.8}Sr_{0.2}MnO_{3-y}$ (space group $R\bar{3}c$, JCPDS entry 53-0058) and Ni_6MnO_8 (space group $Fm\bar{3}m$, JCPDS entry 49-1295) can be observed (Figure S1). Raman spectra of the as-prepared samples reveal active modes at around 492 and 610 cm^{-1}, corresponding to the E_g and A_{1g} modes of the *M*-O in LiMO$_2$ (Figure S2), in good agreement with other work.[38-40] These two peaks intensify with increasing coating, suggesting an increase of the *M*-O bonding at the LSM/LM interface. A weak band at around 630 cm^{-1} in the spectrum for the pristine LM is also observed, which may be attributed to spinel-type ordering, indicating the possibility of spinel defects in the LM structure.[41-42] O 1*s* spectra (XPS, Figure 1c) show peaks at ~ 528.5

and 530.5 - 531 eV, corresponding to *M*-O covalency[43] and Sr-O,[44-45] respectively, which respectively weaken and strengthen with increasing LSM content. The weak peak arising from LM at ~ 530.5 eV can be assigned to Co-O,[46] and Co 2*p* and Ni 2*p* spectra are shown in Figure S3. Mn $2p_{1/2}$ features at 653.1 eV and $2p_{3/2}$ at 641.4 eV are revealed that correspond to MnO_2 (Figure 1d),[47-48] where the oxidation state of Mn is slightly lower on the surface of coated samples, indicating that the Mn within the LSM is likely 3+. As shown in Figure S4, the binding energy of the La 3*d* and Sr 3*d* peaks correspond those for La-O and Sr-O bonding,[36] with these increasing in intensity with increasing LSM. Taken together, the XPS and crystallographic analysis reveal that the crystal structure and composition of LM and LM in LSM2 are similar and that the coating contains Mn^{3+}, indicating the presence of oxygen vacancies in the LSM samples.

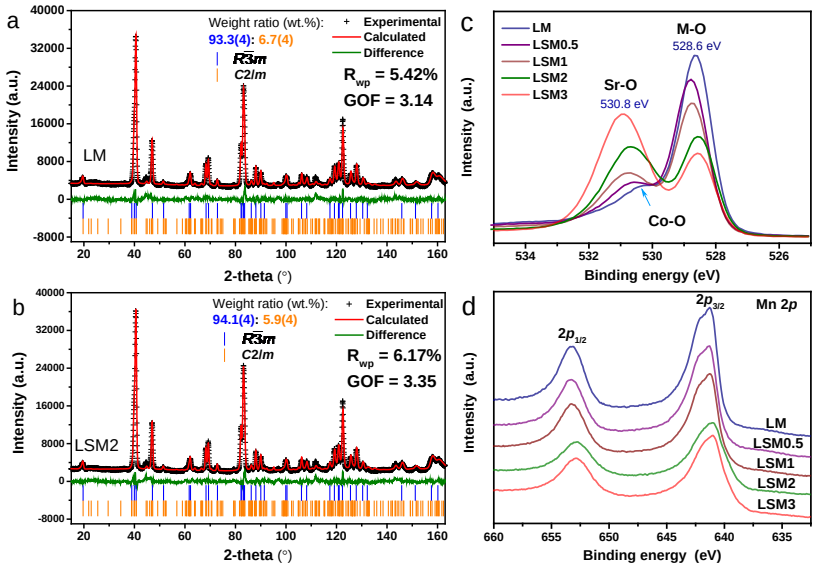

Figure 1. Structural characterization of LM and LSM-coated samples. (a-b) Rietveld refinement profiles using NPD data of LM and LSM2, respectively. (c-d) XPS O 1*s* and Mn 2*p* spectra of the LM and LSM-coated materials.

Microscopy images reveal that the pristine LM is spherical with nanoscale primary particles that are maintained after coating (Figure 2a,e) and that the average particle size of LM and LSM2 is ~ 150-300 nm (Figure 2b,f). As the LSM coating amount increases, the surface of the modified electrode becomes rougher and denser (Figure S5). Transmission electron microscopy (TEM) images of LSM-coated samples show clear evidence of the LSM coating, the thickness of which increased with increased coating amount (Figure S6). Figure 2c,g show high-angle annular dark field scanning TEM (HAADF-STEM) images of LM and LSM that are similar to previous work[29, 49] in which LM exhibits (003) planes with a d-spacing of ~ 0.47 nm. The LSM coating (012) planes can be clearly observed on the Li*M*O_2 particle surface (with (104) planes being observed) the thickness of which is calculated to be 5 ~ 8 nm (Figure 2g and S7). The corresponding fast Fourier transform (FFT) of the image verifies the presence of Li*M*O_2 with a $R\bar{3}m$ space group and LSM with a $R\bar{3}c$ space group (Figure 2d,h). The LSM (012) plane consists of Mn-centred octahedra in which the Mn-O bond length is about 1.96 Å, the same as the *M*-O bond in the LM structure, allowing the formation of a heterostructural connection between the LSM

coating and LM bulk. The O-shared interface between the LSM and LM ensures the stability of the coating over extended cycling. This bonding is consistent with the slightly larger *c* parameter and larger oxygen vacancy of the LSM2 material. Energy dispersive spectroscopy (EDS) was also carried out to determine the elemental distribution of Ni, Co, and Mn, as well as La and Sr within the LSM-coated LM. While Sr could not be clearly identified due to low content, Ni, Co, and Mn are uniformly distributed throughout the particles (Figure 2i and S8) whilst La is only observed in the coating layer, indicating a LSM coating as also confirmed by the EDS line profiles (Figure 2i and S9). It should be noted that the EDS mapping shows a non-uniform distribution of Sr on the surface, which differs from the line profile analysis, which may result from the relatively low Sr content leading to a noisier signal.

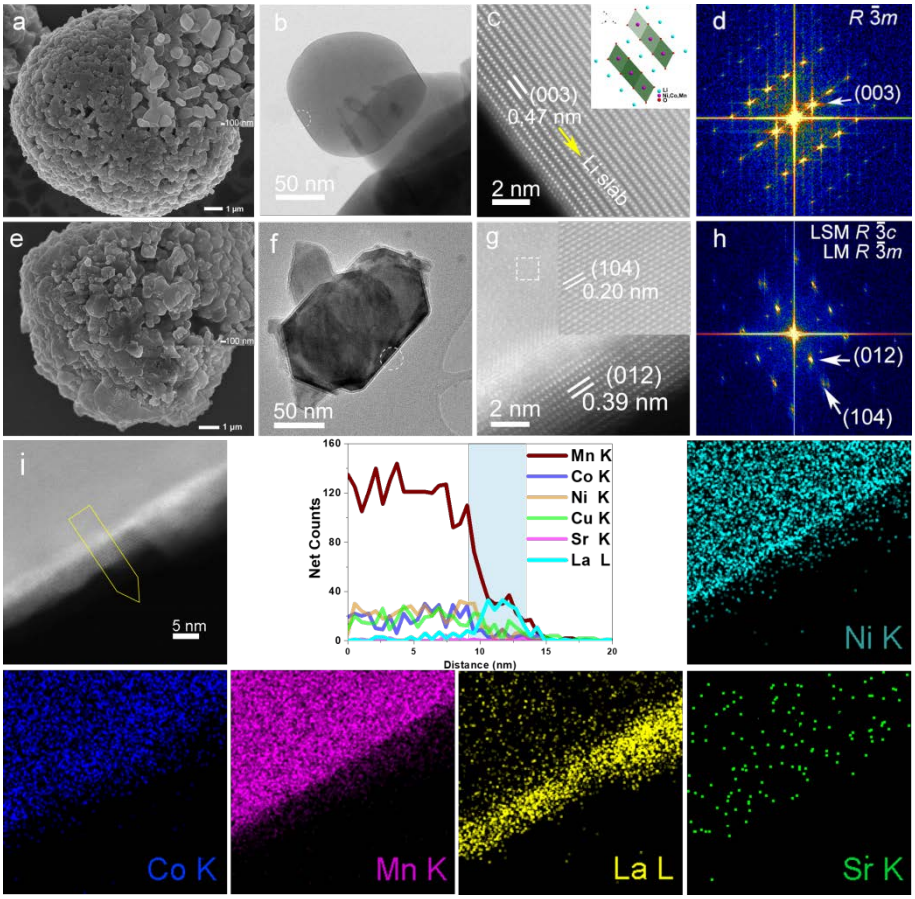

Figure 2. Morphology and local structure of LM and LSM2. Scanning electron microscopy, annular bright-field scanning transmission electron microscopy, and high-angle annular dark field scanning transmission electron microscopy images alongside their corresponding fast Fourier transforms of (a-d) LM and (e-h) LSM2, respectively. (i) Elemental distribution in LSM2 obtained from EDS.

Figure 3a shows the first charge-discharge voltage profiles of coin cells containing the LM or LSM2 electrodes over 2.0 - 4.75 V at 0.1 C (26 mA g^{-1}). Similar to other LLOs, a long plateau at ~ 4.5 V is observed during initial charging, which corresponds to the electrochemical activation of the Li_2MnO_3.[29,50-51] The LM electrode delivers the highest initial discharge capacity of 255.5 mAh g^{-1} and

the lowest Coulombic efficiency of 69%, which increases with the amount of coating, reaching 82% at 3 wt.%. Nevertheless, owing to the inactive LSM content, the coated samples exhibited lower first discharge capacities than the LM electrode. Correspondingly, LSM2 with a 2 wt.% coating is considered the best-performing material, delivering 243.5 mAh g^{-1} and an initial Coulombic efficiency of 80%. Rate capability testing further highlights the advantages of the LSM coating (Figure 3b), where LSM2 exhibits a remarkably higher capacity than LM at all tested rates, and the differences (147 *vs*. 64 mAh g^{-1}) become even more pronounced at 5 C. The initial coulombic efficiency (ICE) of LSM3 is slightly higher (~ 2%) than that of LSM2. Whilst very small and possibly the same within experimental error, this also plausibly may arise from the formation of a thicker heterostructural surface layer, reducing the cathode-electrolyte interface growth and structural disorder, as well as inhibiting oxygen release. Notably, by reducing the *M* (especially Mn) migration and oxygen activity of the electrode, the phase-compatible layer addresses both surface/interface issues including defects and undesirable deposited species,[52] and boosts the electrochemical anionic/cationic redox activity of cation sites (especially O-Mn^{4+}/Li^{+}) and oxygen.[6,53] All LSM-coated electrodes show enhanced cycle stability (Figure 3c), particularly the LSM2 that shows an excellent capacity of 202 mAh g^{-1} (94%) after 200 cycles, in comparison to the uncoated LM electrode with only 84.4 mAh g^{-1} after 200 cycles (48%). Low current (0.2 C) cycling also displays excellent stability with a capacity retention of 97.3% for the coated sample with 2.0 wt.% LSM compared with a capacity retention of 82.1% for the pristine LM (Figure S10). Voltage decay was significantly suppressed by the LSM coating (Figure 3d-g) with both discharge capacity and discharge plateaus of the LM electrode decaying much faster than that of the LSM2 electrode. The LM electrode exhibits a long plateau below 2.8 V which is noticeably suppressed in the LSM2 electrode, and the LSM2 electrode displays higher energy efficiency and retains 80% of initial energy density, double that of the uncoated LM material (40%).

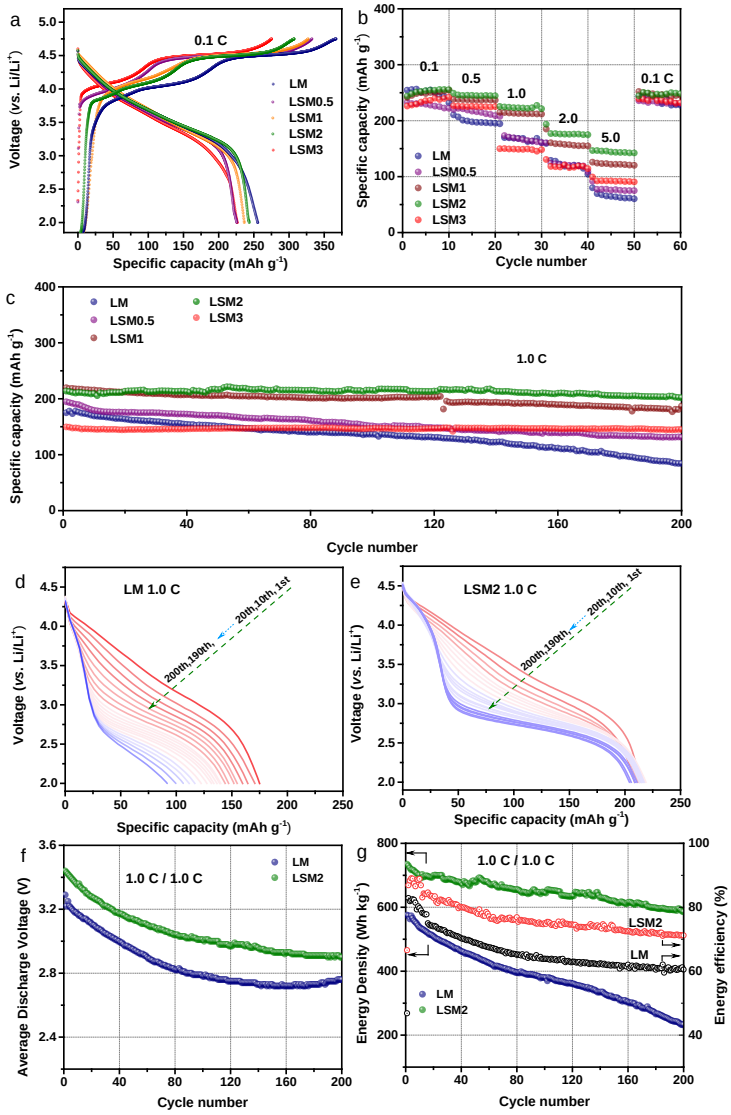

Figure 3. Electrochemical performance of electrodes. (a) First charge-discharge profile at 0.1 C (26 mA g^{-1}); (b) rate capability; (c) cycle performance at 1 C. (d-e) Voltage-discharge capacity profiles of LM and LSM2. (f) Average discharge voltage of LM and LSM2 upon cycling; (g) Energy density and energy efficiency of LM and LSM2 upon cycling calculated based on the activate electrode material mass.

To investigate the enhancement mechanism of the LSM coating, both post-mortem and *in operando* measurements were carried out. It is thought that structural changes of LLOs during cycling such as layered-spinel type transitions,[54] as well as changes in defect concentration[5] and nanovoids,[52] contribute to battery degradation. TEM images of the LM and LSM2 electrodes extracted from coin cells following 200 cycles (Figure 4 and Figure S11, respectively) appear less dense (Figure 4aI and Figure S11I) with nanovoids (yellow dashed line in Figure 4aII and white dashed line in Figure S11II).

Moiré fringes are observed. The LM spinel phase could be identified (white dashed line and inset in Figure 4a) in the uncoated electrode. As shown in the highlighted area in Figure 4aI and Figure S11I, dark parallel bands with a spacing of around 0.8 ~ 1.0 nm are identified, characteristic of dislocations,[55] with partial dislocations noted previously to contribute to LLO voltage fade.[5] A high density of nanovoids in LLOs are also previously identified, as formed by oxygen vacancies following oxygen release from the surface.[4,52] The FFT of the TEM images (Figure 4a and Figure S11) could be indexed to the monoclinic space group *C*2/*m* of the Li_2MnO_3 structure, where red and white dashes indicate nanovoids, with monoclinic (020) lattice fringing (Figure S11II). In comparison, the LSM2 electrode does not show significant defects on the surface (Figure 4b), and the LSM coating remains intact even after 200 cycles. Lattice fringes with a spacing of 0.27 nm (Figure 4bI & II and Figure S11cII) and 0.32 nm (Figure S11cI) arise from *C*2/*m* (-113) and (022) planes, respectively. The TEM images and corresponding FFTs indicate that the bulk LM structure is stable during charge and discharge as protected by the LSM-coating. The bonding between the LM and LSM coating plays a critical role in limiting the formation of defects and nanovoids on the LM surface, as illustrated in Figure 4c and Figure S11b. These results are consistent with our electrochemical analysis that verify reduced voltage fade in the LSM-coated LM.

To assess the lattice deformation and phase changes occurring in the LSM-coated LM during Li extraction and insertion, *in operando* NPD was performed. The Li*M*O_2 012 reflection could be identified in the *in operando* NPD data of the LSM2||$Li_4Ti_5O_{12}$ (LTO) full battery and was analyzed using single peak fitting (Figure 4d and S12). The Li_2MnO_3 phase could not be observed in these data as a result of the large background originating from the hydrogen in the organic electrolyte solvent and separator. The NPD data demonstrate the reversible solid-solution reaction of the LM.[15] The non-linear variation of peak position with derived capacity evidences specific redox reactions, such as the sloping plateau at 2.5 V (*vs.* LTO, equivalent to ~4.0 V *vs.* Li) being smaller than that at 1.5 V (*vs*. LTO), with the higher plateau arising from the Ni^{4+}/Ni^{2+} redox couple and the lower one from Mn^{4+}/Mn^{3+}, in a good agreement with the derived capacity (Figure 3e) and the nominal Ni : Mn ratio.

The O 1*s* XPS spectra (Figure 4e,f) are also used to demonstrate the difference in oxygen on the surface of the cycled LM and LMS2 electrode, with these spectra exhibiting peaks expected for LM.[56-57] A cathode-electrolyte interfacial film may form as a result of the oxidation of organic solvents during the Li_2MnO_3 activation process.[56] For LM (Figure 4e), the peaks located at ~ 530.5, ~ 531.0, ~ 532.0, and 533.0 eV can be assigned to C=O,[58] oxygenated deposited species,[57] carbonate species (CO_3^{2-}),[34] and electrolyte oxidation species,[57] respectively. These results indicate the possible existence of Li_2CO_3 and residue from side reactions on the surface of the LM. In contrast to LM (Figure 4f), the O 1*s* photoelectron spectrum of LSM2 is composed of three features. One can be seen at ~ 529.0 eV and arises from O^{2-} in the transition metal layers and another at ~ 531.0 eV corresponds to the O^{2-} in the LSM structure (Sr-O) as well as oxygenated deposited species. The third peak at ~ 533.0 eV may be attributed to electrolyte oxidation. Moreover, the absence of a peak arising from CO_3^{2-} in the LSM-coated LM suggests a higher level of the surface redox reaction of oxygen compared with that for the LM sample,[52] which contributes to a high discharge capacity and suppresses voltage fade. The XPS data suggest that unwanted side reactions are reduced and the electrolyte decomposition (e.g. Li_2CO_3) at the LM surface suppressed by the LSM coating. As consistent with the O 1*s* spectra, the Mn 2*p*

photoelectron spectra (Figure S13) reveal the reduction of the Mn valence and suppression of Mn dissolution by the LSM coating. The intensity of the Mn 2*p* spectrum for the pristine LM is significantly reduced after long-term cycling, in contrast to that for the cycled LSM2 electrode, where the LSM2 sample has less Mn^{2+} after 200 cycles. These results highlight the difference in cathode-electrolyte interface species in the pristine LM and LSM-coated samples. In particular, the uncoated LM is more likely to generate an undesirable passivation layer, in contrast to the LSM-coated material. Overall, these results indicate that the LSM2 sample has less oxygen release and local structure disorder than the LM sample.

Figure 4. Particle morphology and structure evolution. (a and b) TEM images and corresponding FFT of LM and LSM2 extracted from coin cells after 200 cycles between 2.0 and 4.75 V at 1 C, respectively. (c) The corresponding crystal structure model of the LM electrode; (d) Evolution of the Li*M*O_2 012 reflection in NPD data during cycling of a LSM2||$Li_4Ti_5O_{12}$ battery between 0.5 and 3.3 V (*vs.* LTO) at 0.1 C (0.2 A) during the first two cycles and 0.5 C (1 A) during the third cycle. (e-f) O 1*s* XPS spectra of LM and LSM2 extracted from coin cells after 200 charge-discharge cycles at 1 C rate, respectively.

In summary, the influence of the LSM coating heterostructural with LM on the structural evolution and electrochemical performance of LLOs is illustrated in Figure 5, and has 3 main aspects:

(1) The mitigation of *M* (especially Mn) migration: As illustrated in Figure 5a, the LSM coating is heterostructural with the LM bulk, forming a strong Mn-O-*M* bonding, and reducing the dissolution of Mn, which prevents the layered-spinel transition during cycling. Consequently, the structural disorder in the form of defects, cation vacancies, and unwanted phase transitions are avoided, resulting in enhanced energy and cycling performance;

(2) The mitigation of oxygen release and redox activity in the form of O_2^{n-} or O_2: The Mn-O-*M* bonding protects against oxygen evolution leading to improved first-cycle irreversibility. As depicted in Figure 5a, LSM and LM form a heterostructural interface by sharing O, stabilizing against oxygen release during charging. The formation of defects and nanovoids[52] responsible for the deterioration of electrochemical performance are therefore avoided.

(3) The LSM coating protects against the HF generated from electrolyte decomposition, as similar to other coatings, further reducing Mn dissolution from the LM.

Figure 5b-c summarize the proposed structure evolution of LM and LSM2 during electrochemical cycling. During initial cycling, both LM and LSM2 undergo structural deformation caused by lithium extraction/insertion and oxygen activity. The high levels of oxygen release and cation migration that create issues in the LM including transformation to the spinel phase, as well as the formation of lattice dislocations and nanovoids, are avoided by the LSM coating. Overall, the inactive LSM coating that is heterostructural to the LM stabilizes both O and *M* more effectively than that of other reported coating strategies.

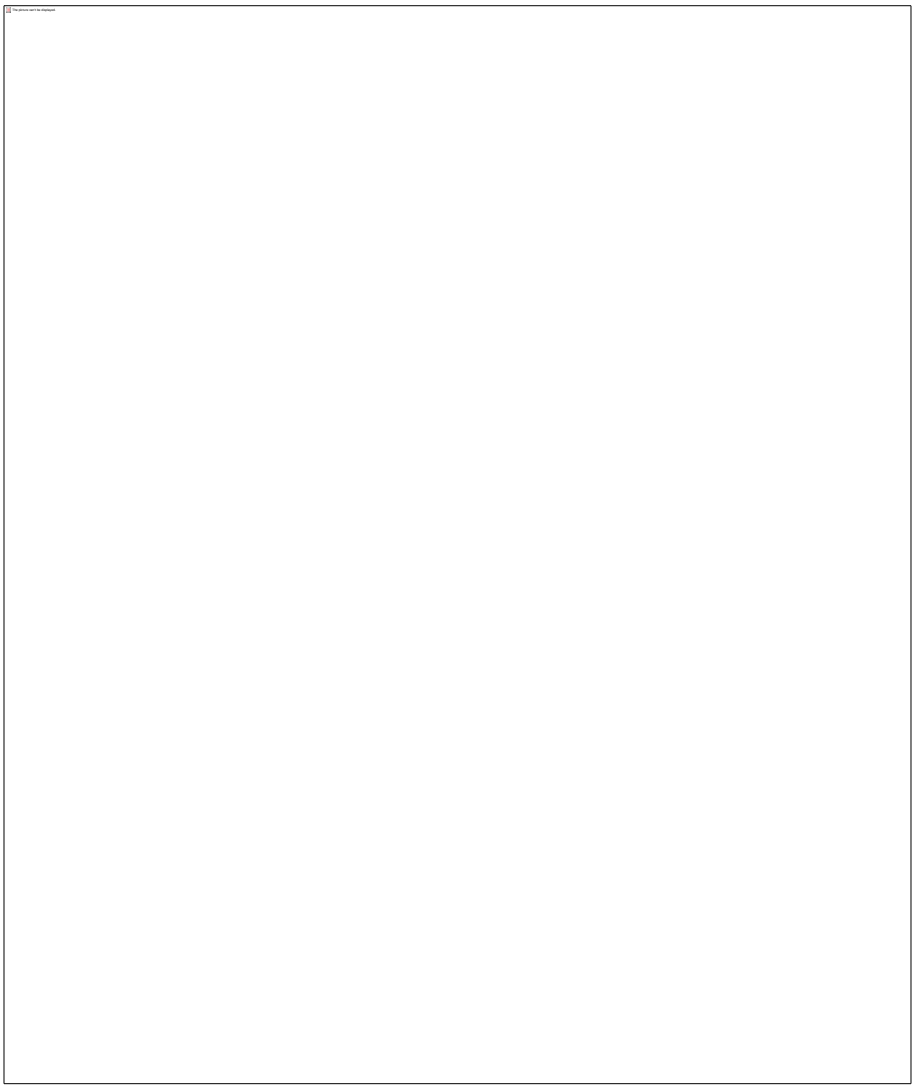

Figure 5. Schematic of mechanism and structural evolution of LSM coated LM showing (a) the heterostructural interface and bonding, and the oxygen release and cation migration in (b) pristine LM, and the marked suppression of these in by the LSM coating (c).

3. Conclusion

A LSM coating is introduced to LM, stabilizing the LM structure. The LSM forms a heterostructural connection with the LM through Mn-O-*M* bonding at the interface. The LSM coating reduces oxygen release during charging, suppresses the formation of defects and nanovoids during cycling, and reduces the dissolution of Mn from the LM. The LSM-coated LM electrode exhibits an enhanced reversible capacity of 202 mAh g^{-1} at 1 C with excellent cycling stability and rate capability. These findings are extendable more broadly to other LLOs and open a new avenue for the surface modification of high-energy and high-voltage electrode materials for metal-ion batteries.

4. Experimental Section

Preparation of Pristine LM: $Li_{1.2}Ni_{0.13}Co_{0.13}Mn_{0.54}O_2$ was synthesized using a co-precipitation method where $[Ni_{0.13}Co_{0.13}Mn_{0.54}](OH)_2$ (2.0 M), $NiSO_4{\cdot}6H_2O$ (Sinopharm Chemical Reagent Co., Ltd; SCRC), $CoSO_4{\cdot}7H_2O$ (SCRC), and $MnSO_4{\cdot}H_2O$ (SCRC) were mixed in a 0.13 : 0.13 : 0.54 molar ratio to which NaOH (SCRC, 4.0 M) and a suitable amount of $NH_3{\cdot}H_2O$ (SCRC) was added during continuous stirring under N_2 at 60 °C. The pH was kept ~ 11. The formed particles were collected, washed with deionized water, and dried at 100 °C for 24 h in a vacuum oven. Finally, the dried precipitate was ball-milled with an adequate amount of Li_2CO_3 (SCRC) and calcined in air at 900 °C for 12 h using a heating ramp of 5 °C min^{-1}.

Surface modification: A stoichiometric mixture of $La(NO_3)_3{\cdot}6H_2O$ (Aldrich, 99%), $Mn(NO_3)_2{\cdot}4H_2O$ (SCRC), $Sr(NO_3)_2$ (Aldrich, 99%), and cetyltrimethyl ammonium bromide (Aldrich) was dissolved in deionized water. To achieve full complexation, the pH was adjusted to ~ 9 using $NH_3{\cdot}H_2O$. The mixture was divided and calcined at 350, 400, 500, and 600 °C for 5 h using heating ramp of 2 °C min^{-1}, with these termed LSMS3, LSMS4, LSMS5, and LSMS6, respectively, and the optimal temperature for the

production of impurity-free material confirmed as 500 °C by examination of these materials using XRPD (Figure S14), XPS (Figure S15-16), and electrochemical performance testing (Figure S17). Subsequently, 0.5, 1, 2, and 3 wt.% LSM were applied to LM at 500 °C to obtain LSM0.5, LSM1, LSM2, and LSM3, respectively.

Material Characterization: X-ray powder diffraction (XRPD) data were collected using a D/Max-2500V/PC instrument equipped with CuKα radiation, λ = 1.5406 Å. The data were recorded in the 2θ range 10-80° at a step size of 0.02° and a scan rate of 2° min^{-1}. Raman micro-spectroscopy studies of the pristine and LSM-coated samples were performed on a Renishaw inVia (UK). The system was equipped with a 532 nm and ~1 mW laser. Scanning electron microscopy (SEM) was performed using a FEI Quanta 200 FEG. The oxidation states of all samples were carried out using X-ray photoelectron spectroscopy (XPS, ESCALAB 250Xi, Thermo Scientific) with Al Kα radiation (1,487.71 eV). Further structural, morphology, and particle size investigations were performed using transmission electron microscopy (TEM) with a JEOL-2010F at 200 kV. *Ex situ* XPS and TEM tests of the active materials was undertaken as extracted from cycled batteries in an argon-filled glove box (O_2 and H_2O concentrations of < 0.1 p.p.m.), which were sealed and transferred to a vacuum oven to evaporate the residual electrolyte. Aberration-corrected high-angle annular dark field (HAADF) scanning TEM (STEM) was performed on a JEM-ARM200F (JEOL) at 200 kV, using an image corrector equipped with a cold field-emission gun and double spherical aberration correctors.

Neutron powder diffraction (NPD) data for LM and LSM2 were collected on the high-resolution neutron powder diffractometer ECHIDNA[59] at the Open Pool Australian Lightwater (OPAL) research reactor at the Australian Nuclear Science and Technology Organization (ANSTO), with a wavelength of 1.6214(4) Å. *In operando* NPD data were collected using WOMBAT,[60] the high-intensity neutron powder diffractometer at the OPAL research reactor at ANSTO. A cylindrical rolled type LSM2||$Li_4Ti_5O_{12}$ cell was prepared at the School of Chemistry and Pharmaceutical Sciences, Guangxi Normal University and inserted into a polymer coated aluminum pouch casing for the *in operando* NPD experiment. Electrodes were prepared from slurries containing 93 wt.% of active material, 2 wt.% acetylene black, 2 wt.% super P, and 3 wt.% polyvinylidene fluoride binder. The areal densities were ~ 5.5 mg cm^{-2} and ~ 7.0 mg cm^{-2} for LSM2 and $Li_4Ti_5O_{12}$, respectively. Conventional Celgard 2400 was used as the separator. The cell was ~ 6 cm high with a diameter ~ 2 cm and filled with ~15 g of electrolyte comprising 1 M $LiPF_6$ in a 1: 1: 1 volume ratio of ethylene carbonate: ethylmethyl carbonate: diethyl carbonate. The battery is shown in Figure S12. A neutron beam with a wavelength of 2.4213(2) Å was used, as determined using the $La^{11}B_6$ NIST standard reference material 660b. During galvanostatically charge-discharge cycling using a potentiostat/galvanostat (Autolab PG302N) at currents of 0.2 and 1.0 A (0.1 and 0.5 C rates, respectively), NPD data of the battery were collected in the 2ϑ angular range 17.25-135.75 with an exposure time of 5 min per pattern.

Electrochemical Tests: Electrodes were prepared from a slurry of active material, super P and poly(vinylidene fluoride) in a weight ratio of 8: 1: 1 using N-Methyl pyrrolidone as solvent. The slurry

was cast onto an aluminum current collector, followed by drying at 80 °C for 12 h in a vacuum oven. The typical active material loading was about 4 mg cm^{-2}. CR2032 coin cells were assembled in an argon-filled glove box with lithium metal foil as counter electrode and Celgard 2400 as separator. 1 M $LiPF_6$ electrolyte solution was dissolved in ethylene carbonate, ethyl-methyl carbonate, and diethyl carbonate (1: 1: 1 vol%). Battery testing was performed using a LAND CT-2001A instrument (Wuhan, China) at 25 °C. The cells were charged-discharged for several cycles at various currents in the range 2.00-4.75 V, with the C-rate defined based on 1 C = 260 mA g^{-1}. Cyclic voltammetry (CV) was performed using a Zahner IM6 electrochemical workstation at a scan rate of 0.1 mV s^{-1} in the range 2.0-4.75 V.

Supporting Information

Supporting Information is available from the Wiley Online Library or from the author.

Acknowledgements

This work was supported by funding from the National Natural Science Foundation of China (NSFC, 51474110 and 51802357) and Natural Science Foundation of Hubei Province (2018CFB192 and 2018CFB237), Science and Technology Research Program of Young Talent Project of Hubei Provincial Department of Education (Q20172904). Dr. S. Hu acknowledges the China Scholarship Council (CSC) for their scholarships (Grant No. 201608420205). The authors are also grateful to the support of the Australian Research Council (ARC) through the funded projects (FT160100251, LP160101629, and DE190100504). The operational support of ANSTO staff contributing to the collection of neutron powder diffraction data is highly appreciated. The authors thank Dr. Tania Silver for her critical review of the manuscript and valuable feedback.

Received: ((will be filled in by the editorial staff))
Revised: ((will be filled in by the editorial staff))
Published online: ((will be filled in by the editorial staff))

References

[1] M. M. Thackeray, S.-H. Kang, C. S. Johnson, J. T. Vaughey, R. Benedek, S. A. Hackney, *J. Mater. Chem.* **2007**, *17*, 3112.

[2] S. Hu, A. S. Pillai, G. Liang, W. K. Pang, H. Wang, Q. Li, Z. Guo, *Electrochem. Energ. Rev.* **2019**, *2*, 277.

[3] A. K. Shukla, Q. M. Ramasse, C. Ophus, H. Duncan, F. Hage, G. Chen, *Nat. Commun.* **2015**, *6*, 8711.

[4] E. Hu, X. Yu, R. Lin, X. Bi, J. Lu, S. Bak, K.-W. Nam, H. L. Xin, C. Jaye, D. A. Fischer, K. Amine, X.Q. Yang *Nat. Energy* **2018**, *3*, 690.

[5] A. Singer, M. Zhang, S. Hy, D. Cela, C. Fang, T. A. Wynn, B. Qiu, Y. Xia, Z. Liu, A. Ulvestad, N. Hua, J. Wingert, H. Liu, M. Sprung, A. V. Zozulya, E. Maxey, R. Harder, Y. S. Meng, O. G. Shpyrko, *Nat. Energy* **2018**, *3*, 641.

[6] K. Luo, M. R. Roberts, R. Hao, N. Guerrini, D. M. Pickup, Y.-S. Liu, K. Edström, J. Guo, A. V. Chadwick, L. C. Duda, P.G. Bruce, *Nat. Chem.* **2016**, *8*, 684.

[7] G. Assat, D. Foix, C. Delacourt, A. Iadecola, R. Dedryvère, J.-M. Tarascon, *Nat. Commun.* **2017**, *8*, 2219.

[8] F. Fu, J. Tang, Y. Yao, M. Shao, *ACS Appl. Mater. Interfaces* **2016**, *8*, 25654.

[9] X. Yuan, Q.-j. Xu, X. Liu, W. Shen, H. Liu, Y. Xia, *Electrochim. Acta* **2016,** *207*, 120.

[10] R. Yu, G. Wang, M. Liu, X. Zhang, X. Wang, H. Shu, X. Yang, W. Huang, *J. Power Sources* **2016**, *335*, 65.

[11] F. Wu, J. Liu, L. Li, X. Zhang, R. Luo, Y. Ye, R. Chen, *ACS Appl. Mater. Interfaces* **2016**, *8*, 23095.

[12] S. Kalluri, M. Yoon, M. Jo, H. K. Liu, S. X. Dou, J. Cho, Z. Guo, *Adv. Mater.* **2017**, *29*, 1605807.

[13] J. Li, R. Shunmugasundaram, R. Doig, J. R. Dahn, *Chem. Mater.* **2015**, *28*, 162.

[14] A. Devaraj, M. Gu, R. Colby, P. Yan, C. M. Wang, J. M. Zheng, J. Xiao, A. Genc, J. G. Zhang, I. Belharouak, D. Wang, K. Amine, S. Thevuthasan, *Nat. Commun.* **2015**, *6*, 8014.

[15] W. K. Pang, H.-F. Lin, V. K. Peterson, C.-Z. Lu, C.-E. Liu, S.-C. Liao, J.-M. Chen, *Chem. Mater.* **2017**, *29*, 10299.

[16] J. Lu, Z. Chen, Z. Ma, F. Pan, L. A. Curtiss, K. Amine, *Nat. Nanotechnol.* **2016**, *11*, 1031.

[17] F. Lin, I. M. Markus, D. Nordlund, T.-C. Weng, M. D. Asta, H. L. Xin, M. M. Doeff, *Nat. Commun.* **2014**, *5*, 3529.

[18] J. Zheng, S. Myeong, W. Cho, P. Yan, J. Xiao, C. Wang, J. Cho, J. G. Zhang, *Adv. Energy Mater.* **2017**, *7*, 1601284.

[19] H. Liu, D. Qian, M. G. Verde, M. Zhang, L. Baggetto, K. An, Y. Chen, K. J. Carroll, D. Lau, M. Chi, G.M. Veith, Y.S. Meng, *ACS Appl. Mater. Interfaces* **2015**, *7*, 191890.

[20] B. Li, J. Wang, Z. Cao, P. Zhang, J. Zhao, *J. Power Sources* **2016**, *325*, 84.

[21] X. Zhang, I. Belharouak, L. Li, Y. Lei, J. W. Elam, A. Nie, X. Chen, R. S. Yassar, R. L. Axelbaum, *Adv. Energy Mater.* **2013**, *3*, 1299.

[22] Y. K. Sun, M. J. Lee, C. S. Yoon, J. Hassoun, K. Amine, B. Scrosati, *Adv. Mater.* **2012**, *24*, 1192.

[23] K. Gao, S.-X. Zhao, S.-T. Guo, C.-W. Nan, *Electrochim. Acta* **2016**, *206*, 1.

[24] D. R. Chen, F. Zheng, L. Li, M. Chen, X. X. Zhong, W. S. Li, L. Lu, *J. Power Sources* **2017**, *341*, 147.

[25] B. Song, W. Li, S.-M. Oh, A. Manthiram, *ACS Appl. Mater. Interfaces* **2017**, *9*, 9718.

[26] X. Liu, Q. Su, C. Zhang, T. Huang, A. Yu, *ACS Sustainable Chem. Eng.* **2016**, *4*, 255.

[27] D. Chen, W. Tu, M. Chen, P. Hong, X. Zhong, Y. Zhu, Q. Yu, W. Li, *Electrochim. Acta* **2016**, *193*, 45.

[28] M. Xu, Z. Chen, H. Zhu, X. Yan, L. Li, Q. Zhao, *J. Mater. Chem. A* **2015**, *3*, 13933.

[29] W. Liu, P. Oh, X. Liu, S. Myeong, W. Cho, J. Cho, *Adv. Energy Mater.* **2015**, *5*, 1500274.

[30] J. Q. Li, P. Xiao, *J. Eur. Ceram. Soc.* **2001**, *21*, 659.

[31] A. C. Co, V. I. Birss, *J. Phys. Chem. B* **2006**, *110*, 11299.

[32] G. Zhao, Y. Lin, T. Zhou, Y. Lin, Y. Huang, Z. Huang, *J. Power Sources* **2012**, *215*, 63.

[33] T. Shi, Y. Dong, C.-M. Wang, F. Tao, L. Chen, *J. Power Sources* **2015**, *273*, 959.

[34] H. Koga, L. Croguennec, M. Ménétrier, P. Mannessiez, F. Weill, C. Delmas, *J. Power Sources* **2013**, *236*, 250.

[35] J. Hong, H.-D. Lim, M. Lee, S.-W. Kim, H. Kim, S.-T. Oh, G.-C. Chung, K. Kang, *Chem. Mater.* **2012**, *24*, 2692.

[36] H.-Q. Wang, F.-Y. Lai, Y. Li, X.-H. Zhang, Y.-G. Huang, S.-J. Hu, Q.-Y. Li, *Electrochimica Acta* **2015**, 177, 290.

[37] K. A. Jarvis, Z. Deng, L. F. Allard, A. Manthiram, P. J. Ferreira, *Chem. Mater.* **2011**, *23*, 3614.

[38] Y. W. Denis, K. Yanagida, *J. Electrochem. Soc.* **2011**, *158*, A1015.

[39] P. K. Nayak, J. Grinblat, M. Levi, E. Levi, S. Kim, J. W. Choi, D. Aurbach, *Adv. Energy Mater.* **2016**, *6*, 1502398.

[40] S. Hy, F. Felix, J. Rick, W.-N. Su, B. J. Hwang, *J. Am. Chem. Soc.* **2014**, *136*, 999.

[41] R. Baddour-Hadjean, J.P. Pereira-Ramos, *Chem. Rev.* **2010**, *110*, 1278.

[42] W. Huang, R. Frech, *J. Power Sources* **1999**, *81-82*, 616.

[43] A. W. Moses, H. G. G. Flores, J.-G. Kim, M. A. Langell, *Appl. Surf. Sci.* **2007**, *253*, 4782.

[44] J.-C. Dupin, D. Gonbeau, P. Vinatier, A. Levasseur, *Phys. Chem. Chem. Phys.* **2000**, 2, 1319.

[45] P.-Y. Peng, Y.-C. Tsai, J.-T. Yeh, Y.-S. Lin, C.-M. Huang, *Aerosol Air Qual. Res.* **2015**, *15*, 1662.

[46] L. Chen, X. Zuo, L. Zhou, Y. Huang, S. Yang, T. Cai, D. Ding, *Chem. Eng. J.* **2018**, *345*, 364.

[47] R. P. Qing, J. L. Shi, D. D. Xiao, X. D. Zhang, Y. X. Yin, Y. B. Zhai, L. Gu, Y. G. Guo, *Adv. Energy Mater.* **2016**, *6*, 1501914.

[48] N. Treuil, C. Labrugère, M. Menetrier, J. Portier, G. Campet, A. Deshayes, J.-C. Frison, S.-J. Hwang, S.-W. Song, J.-H. Choy, *J. Phys. Chem. B* **1999**, *103*, 2100.

[49] M. Chen, D. Chen, Y. Liao, X. Zhong, W. Li, Y. Zhang, *ACS Appl. Mater. Interfaces* **2016**, *8*, 4575.

[50] T. A. Arunkumar, Y. Wu, A. Manthiram, *Chem. Mater.* **2007**, *19*, 3067.

[51] S. Kim, W. Cho, X. Zhang, Y. Oshima, J. W. Choi, *Nat. Commun.* **2016**, *7*, 13598.

[52] P. Yan, J. Zheng, Z.-K. Tang, A. Devaraj, G. Chen, K. Amine, J.-G. Zhang, L.-M. Liu, C. Wang, *Nat. Nanotechnol.* **2019**, *14*, 602.

[53] J. Hong, W.E. Gent, P. Xiao, K. Lim, D.H. Seo, J. Wu, P.M. Csernica, C.J. Takacs, D. Nordlund, C.J. Sun, K.H. Stone, D. Passarello, W. Yang, D. Prendergast, G. Ceder, M.F. Toney, W.C. Chueh, *Nat. Mater.* **2019**, *18*, 256

[54] D. Mohanty, J. Li, D. P. Abraham, A. Huq, E. A. Payzant, D. L. Wood, C. Daniel, *Chem. Mater.* **2014**, *26*, 6272.

[55] A. B. Naden, K. J. O'Shea, D. A. MacLaren, *Nanotechnology* **2018**, *29*, 165704.

[56] N. Yabuuchi, K. Yoshii, S.-T. Myung, I. Nakai, S. Komaba, *J. Am. Chem. Soc.* **2011**, *133*, 4404.

[57] M. Sathiya, G. Rousse, K. Ramesha, C. P. Laisa, H. Vezin, M. T. Sougrati, M.-L. Doublet, D. Foix, D. Gonbeau, W. Walker, A. S. Prakash, M. Ben Hassine, L. Dupont, J-M. Tarascon, *Nat. Mater.* **2013**, *12*, 827.

[58] S. Yuan, Y. B. Liu, D. Xu, D. L. Ma, S. Wang, X. H. Yang, Z. Y. Cao, X. B. Zhang, *Adv. Sci.* **2015**, *2*, 1400018.

[59] C.-J. Chen, W. K. Pang, T. Mori, V. K. Peterson, N. Sharma, P.-H. Lee, S.-h. Wu, C.-C. Wang, Y.-F. Song, R.-S. Liu, *J. Am. Chem. Soc.* **2016**, *138*, 8824.

[60] W. K. Pang, V. K. Peterson, *J. Appl. Crystallogr.* **2015**, *48*, 280.

A facile surface engineering strategy is used to introduce **a phase-compatible $La_{0.8}Sr_{0.2}MnO_{3-y}$ (LSM) coating** with an $R\bar{3}c$ hexagonal symmetry to a $Li_{1.2}Ni_{0.13}Co_{0.13}Mn_{0.54}O_2$ (LM) cathode material with hexagonal $R\,\bar{3}\,m$ symmetry. The electrode bulk structure is stabilized by the coating by the heterostructural Mn-O-*M* (Ni, Co, Mn) bonding at the LSM/LM interface.

Keyword: lithium-ion batteries; Li-rich layered oxide; surface-coating; voltage fade; metal ion migration

Sijiang Hu, Yu Li, Yuhua Chen, Jiming Peng, Tengfei Zhou, Wei Kong Pang,* Christophe Didier, Vanessa K. Peterson, Hongqiang Wang,* Qingyu Li, and Zaiping Guo*

Title: Insight of A Phase Compatible Surface-Coating for Long-Durable Li-rich Layered Oxide Cathode

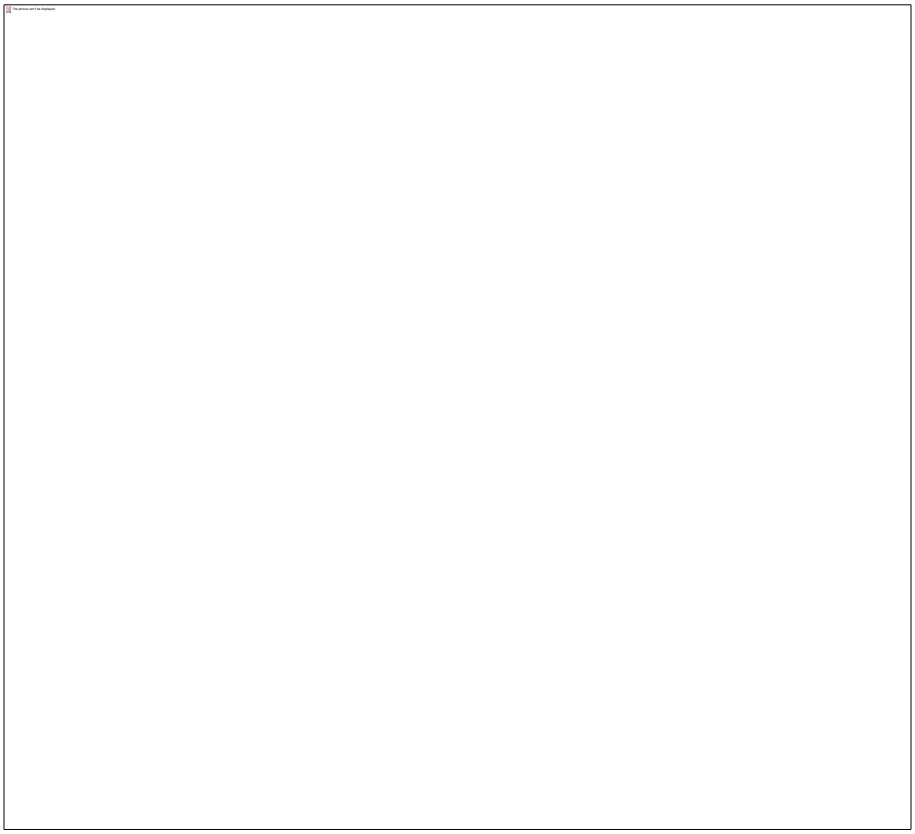

Supplementary Information for

Insight of A Phase Compatible Surface-Coating for Long-Durable Li-rich Layered Oxide Cathode

Sijiang Hu, Yu Li, Yuhua Chen, Jiming Peng, Tengfei Zhou, Wei Kong Pang, Christophe Didier, Vanessa K. Peterson, Hongqiang Wang,* Qingyu Li, and Zaiping Guo**

Dr. S. J. Hu, J. M. Peng, Prof. H. Q. Wang
Hubei Key Laboratory for Processing and Application of Catalytic Materials, College of Chemistry and Chemical Engineering,
Huanggang Normal University, Huanggang 438000, P.R. China
E-mail: whq74@126.com

Dr. S. J. Hu, Dr. T. F. Zhou, Dr. W. K. Pang, Dr. C. Didier, Prof. V. K. Peterson, Prof. Z. P. Guo
Institute for Superconducting and Electronic Materials, School of Mechanical, Materials, Mechatronic, and Bio-medical Engineering,
University of Wollongong, NSW 2500, Australia
E-mail: wkpang@uow.edu.au; zguo@uow.edu.au

Y. Li, Y. H. Chen, J. M. Peng, Prof. H. Q. Wang, Prof. Q. Y. Li
Guangxi Key Laboratory of Low Carbon Energy Materials, School of Chemistry and Pharmaceutical Sciences,
Guangxi Normal University, Guilin 541004, P.R. China

Dr. C. Didier, Prof. V. K. Peterson
Australian Centre for Neutron Scattering, Australian Nuclear Science and Technology Organization, Locked Bag 2001, Kirrawee DC, New South Wales 2232, Australia

Table S1. Crystallographic details of LM and LSM2.

LM

Space group: $R\bar{3}m$

Lattice parameters: a = 2.8512(3) Å, c = 14.2351(6) Å, V= 100.22(1) Å^3

Atom	Wyckoff position	*x*	*y*	*z*	Uiso (Å^2)	Occupancy (x 100%)
Li	3*b*	0	0	1/2	0.0081(3)	0.987
Ni						0.013
Li	3*a*	0	0	0	0.0081(3)	0.013
Ni						0.020(3)
Mn						0.578(2)
Co						0.389(1)
O	6*c*	0	0	0.25861(7)	0.0081(3)	0.999(15)

LSM2

Space group: $R\bar{3}m$

Lattice parameters: a = 2.8513(3) Å, c = 14.2371(7) Å, V= 100.24(1) Å^3

Atom	Wyckoff position	*x*	*y*	*z*	Uiso (Å^2)	Occupancy (x100%)
Li	3*b*	0	0	1/2	0.0077(4)	0.987
Ni						0.013
Li	3*a*	0	0	0	0.0077(4)	0.013
Ni						0.020(3)
Co						0.578(2)
Mn						0.389(1)
O	6*c*	0	0	0.25861(6)	0.0077(4)	0.986(14)

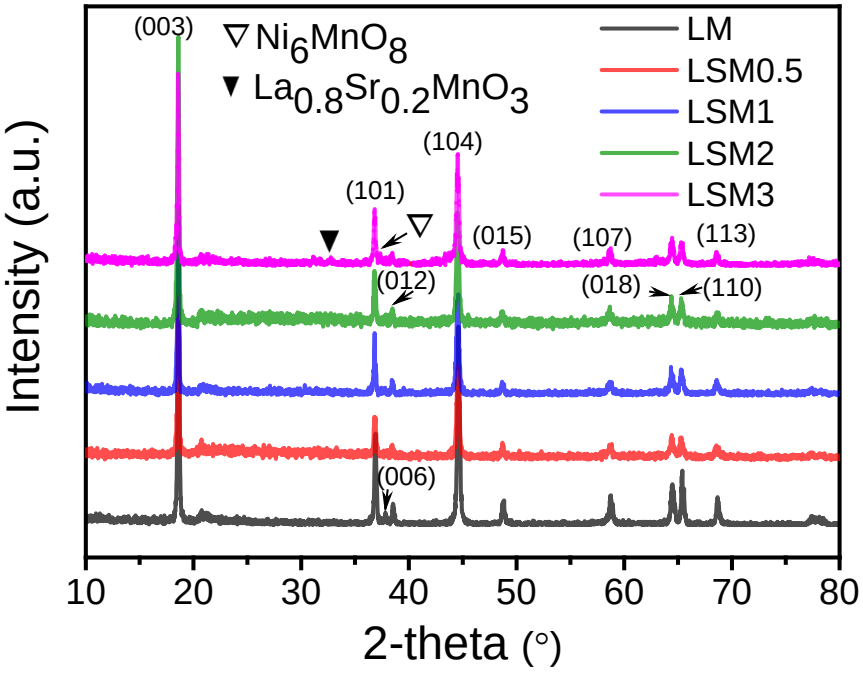

Figure S1. XRPD data of the pristine LM and LSM-coated LM.

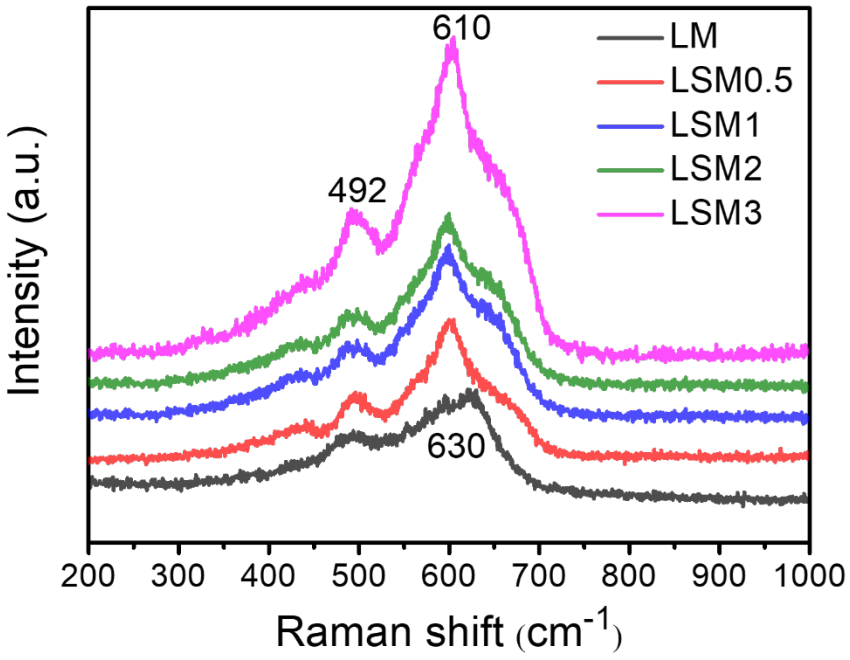

Figure S2. Raman spectra of the pristine LM and LSM-coated LM.

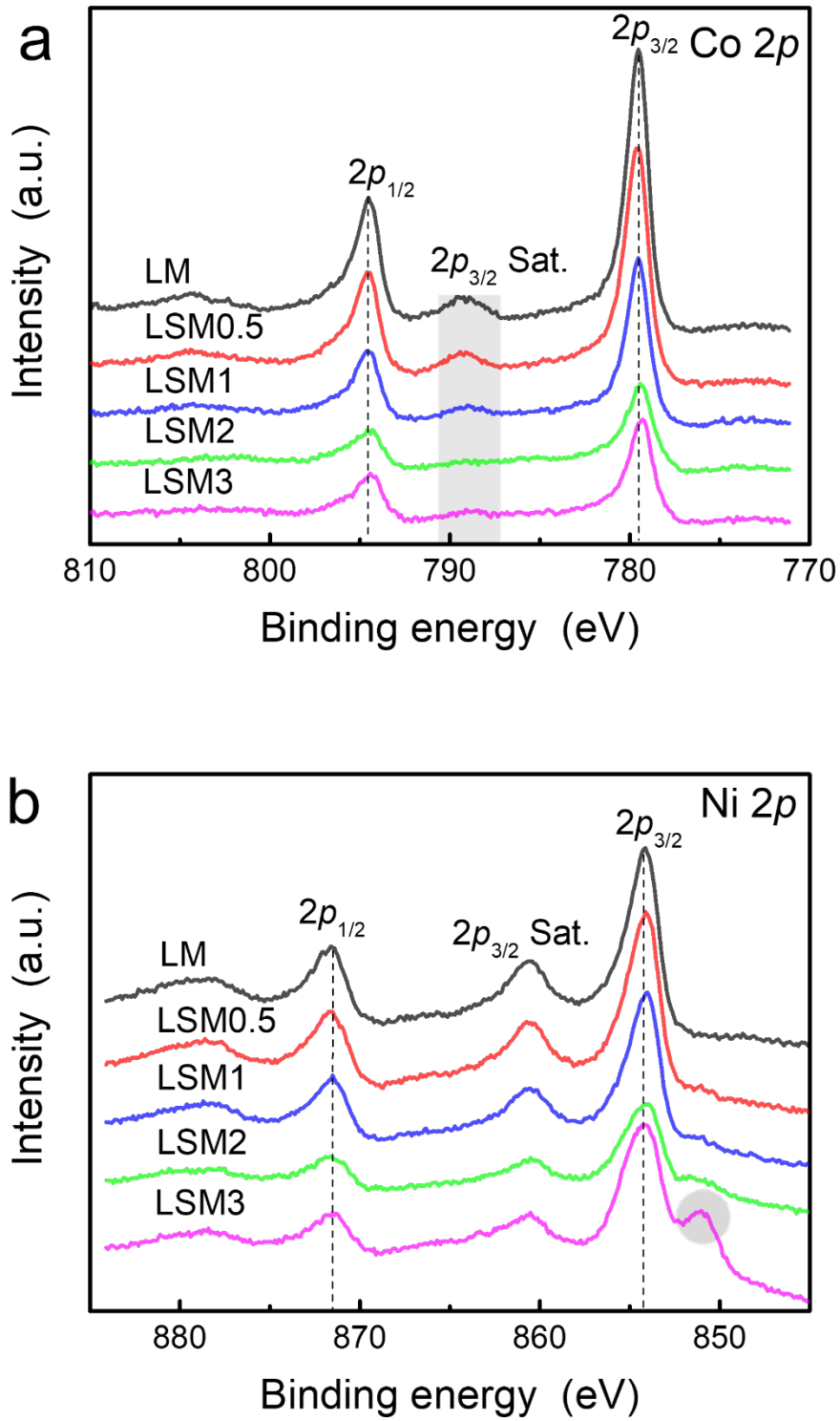

Figure S3. XPS spectra. (a) Co 2*p* and (b) Ni 2*p* spectra of pristine LM and LSM-modified LM.

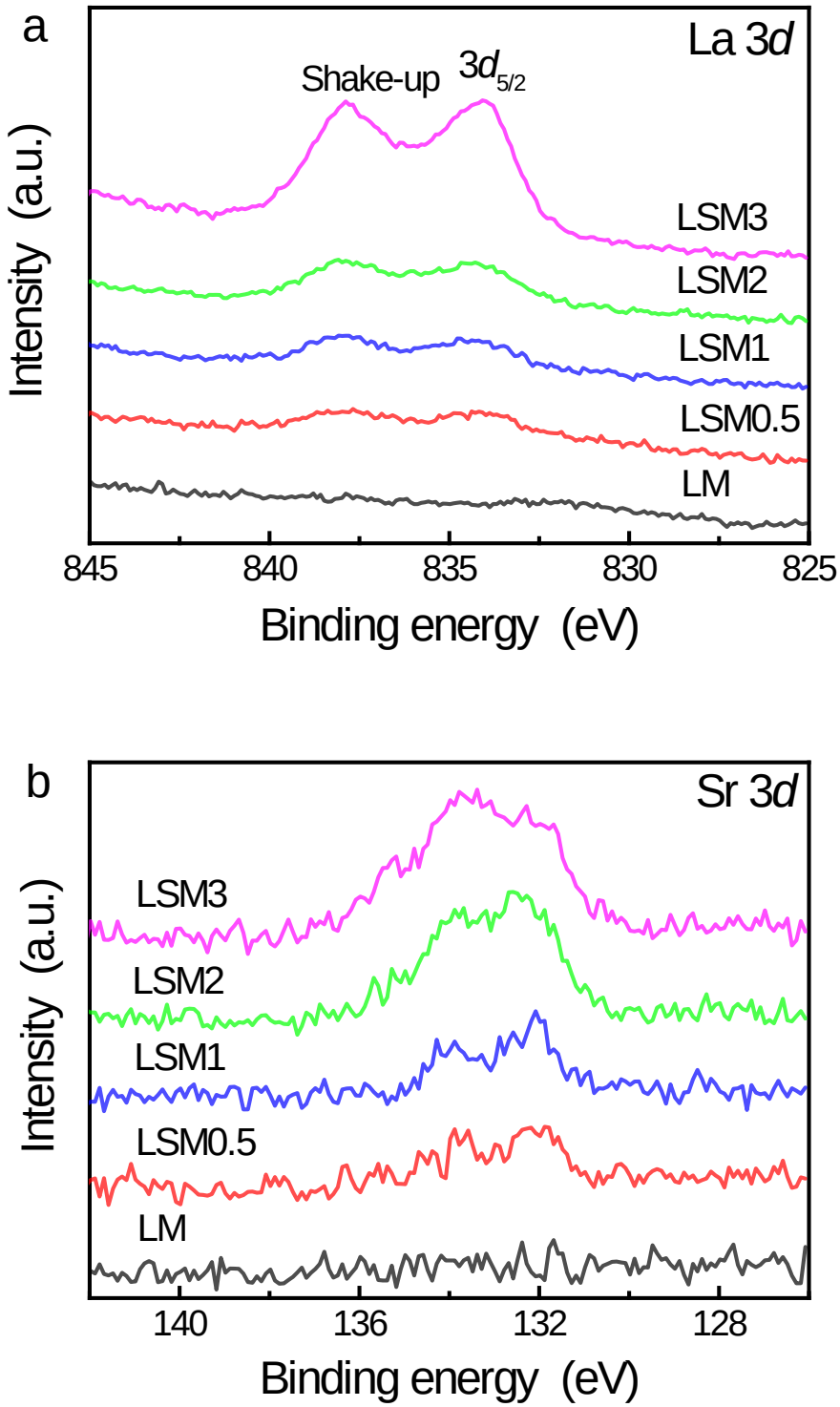

Figure S4. XPS spectra. (a) La 3*d* and (b) Sr 3*d* spectra of pristine LM and LSM-coated LM.

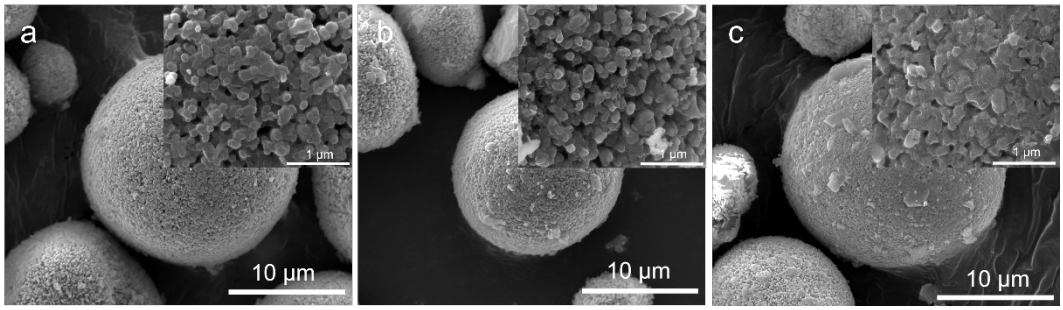

Figure S5. SEM images of the LSM-coated samples. (a) LSM0.5; (b) LSM1; (c) LSM3.

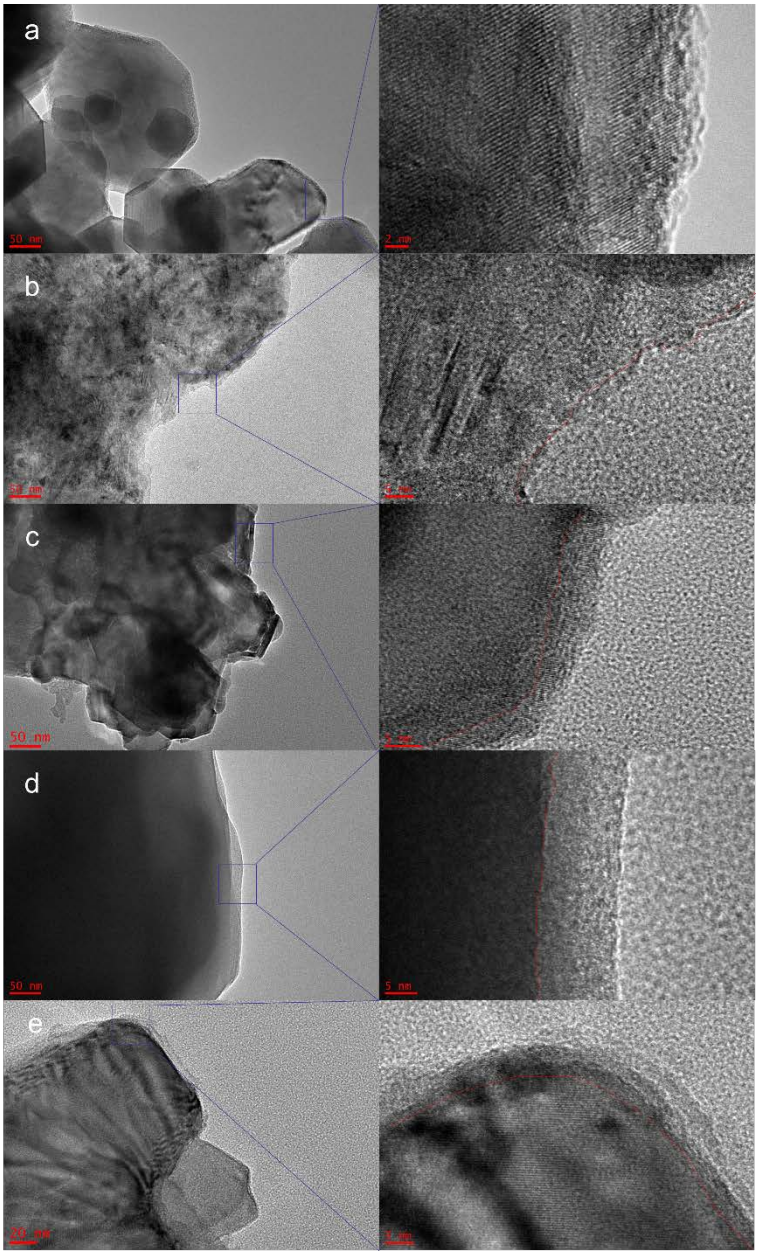

Figure S6. TEM images of the pristine and LSM-coated samples. (a) LM; (b) LSM0.5; (c) LSM1; (d) LSM2; (e) LSM3.

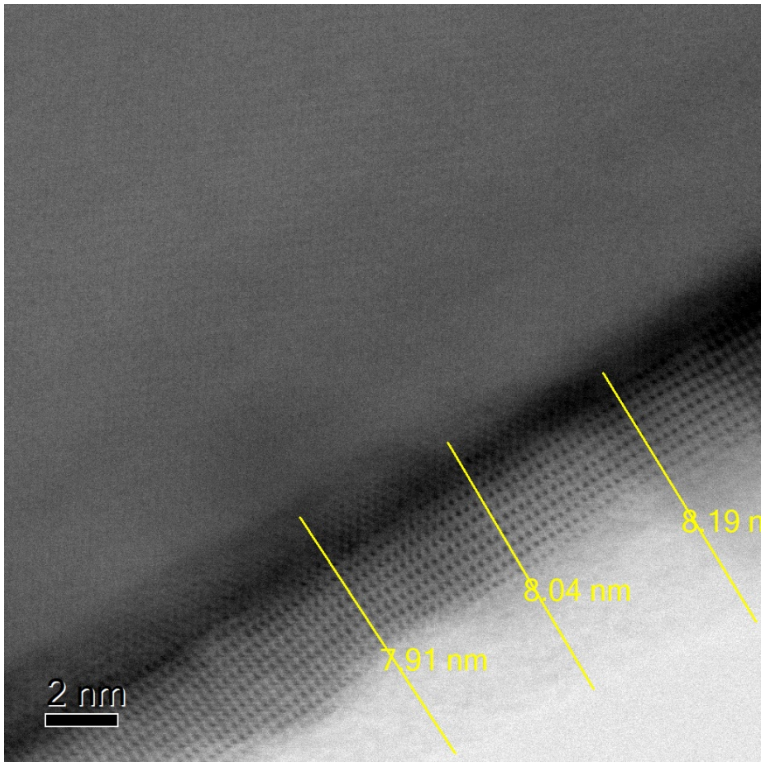

Figure S7. Annular bright-field scanning transmission electron microscopy (ABF-STEM) image of LSM2.

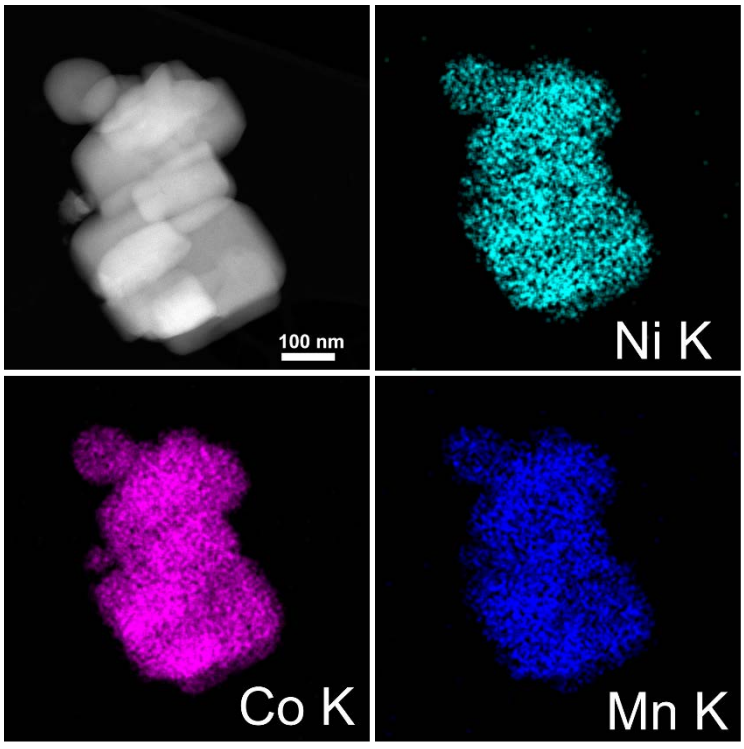

Figure S8. Elemental mapping of LM obtained from EDS.

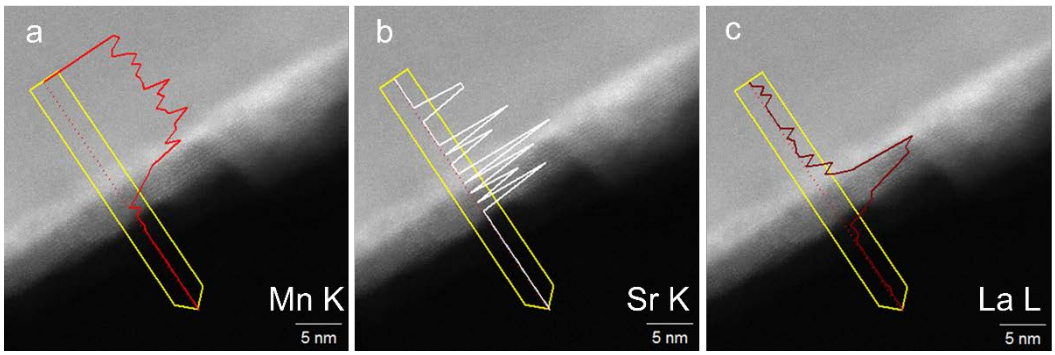

Figure S9. EDS line profiles of LSM2 for Mn, Sr, and La.

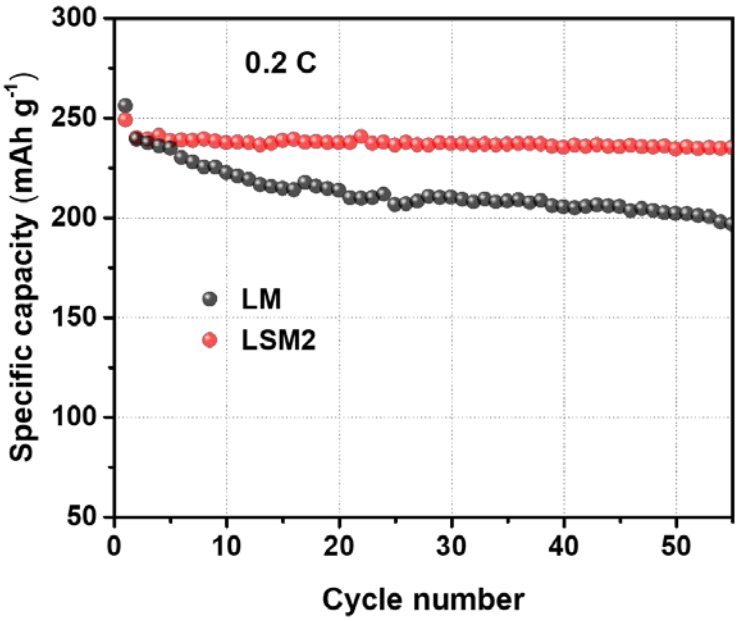

Figure S10. Cycling performance of LM and LSM2 after a first cycle at 0.1 C and then at 0.2 C.

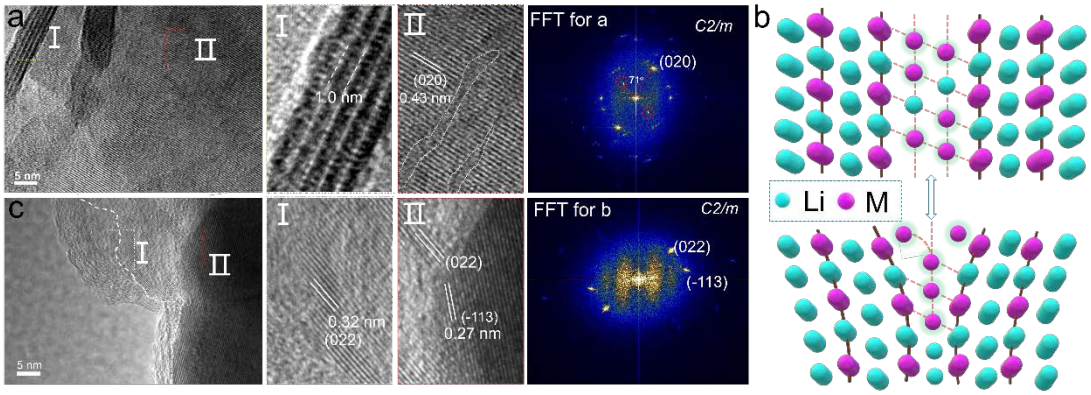

Figure S11. TEM images and their FFT (a,c) of LM (top) and LSM2 (bottom), and corresponding structural models (b) of LM electrodes extracted from coin cells after 200 cycles over 2.0 - 4.75 V.

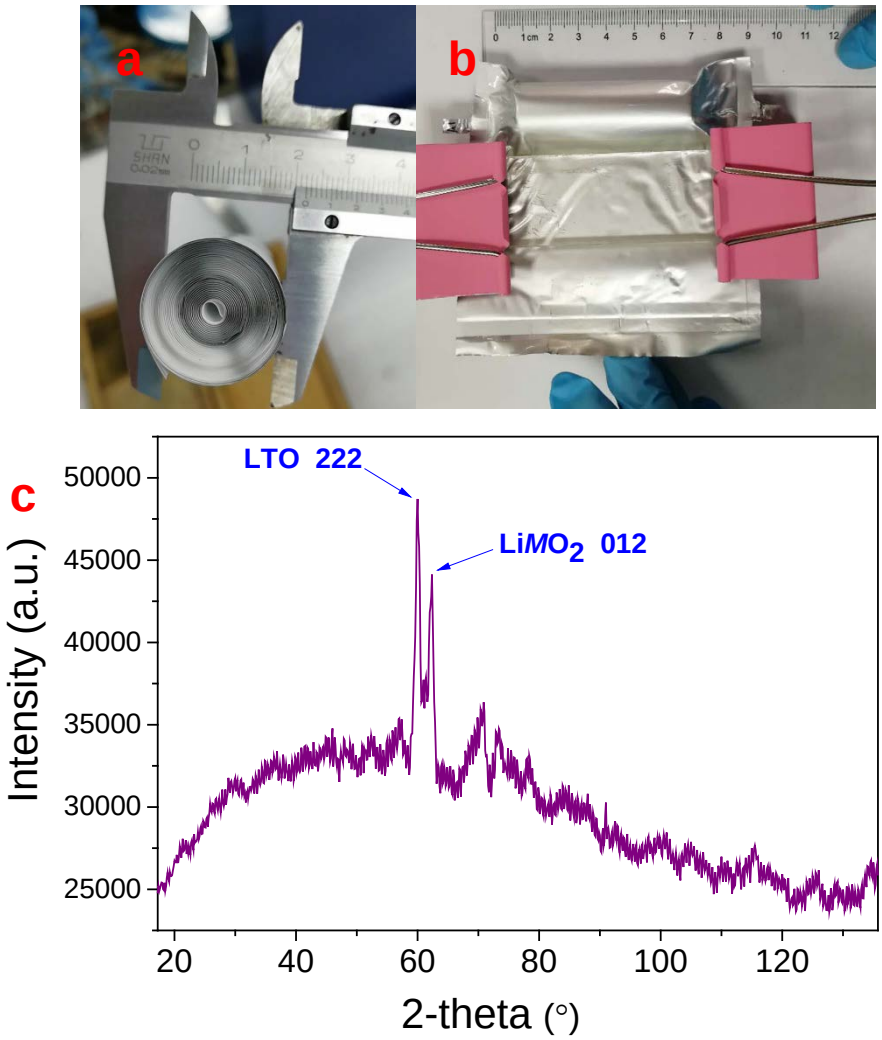

Figure S12. Cylindrical rolled LSM2||$Li_4Ti_5O_{12}$ battery used for *in operando* NPD analysis showing the as-prepared battery core without (a) and with (b) electrolyte. (c) The first NPD pattern in the *in operando* dataset.

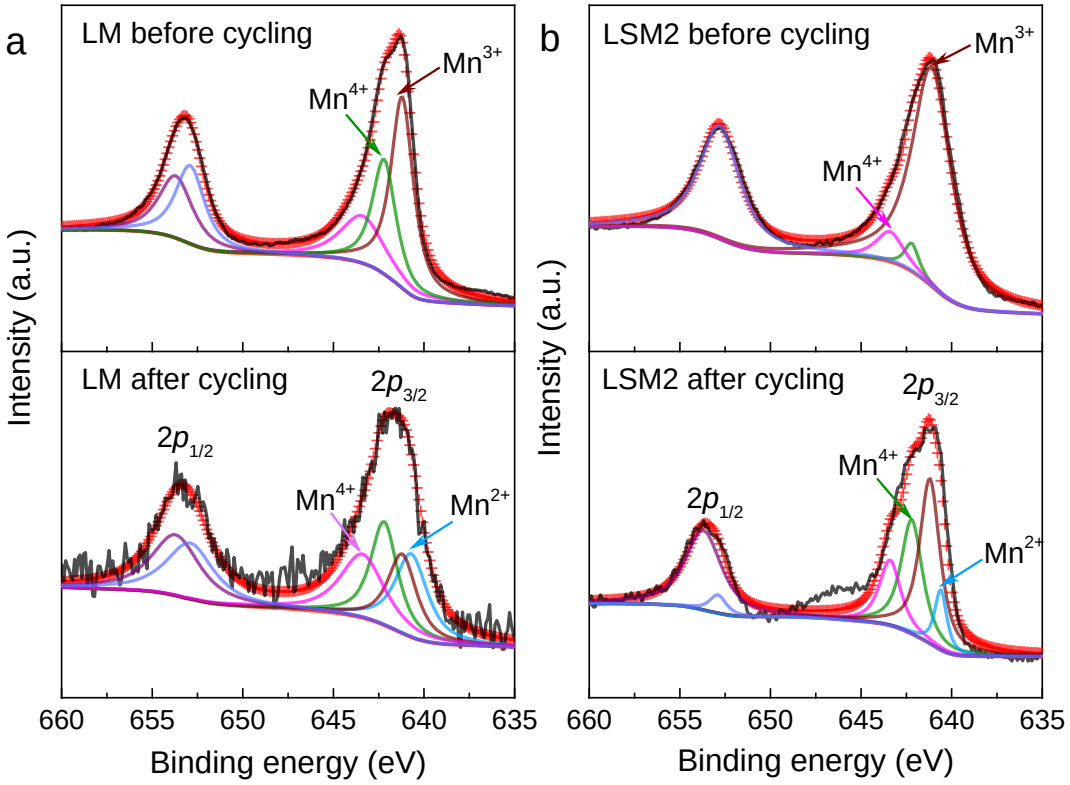

Figure S13. Mn 2*p* XPS data of the LM (a) and LSM2 (b) electrodes before cycling and extracted from coin cells after 200 charge-discharge cycles at 1 C.

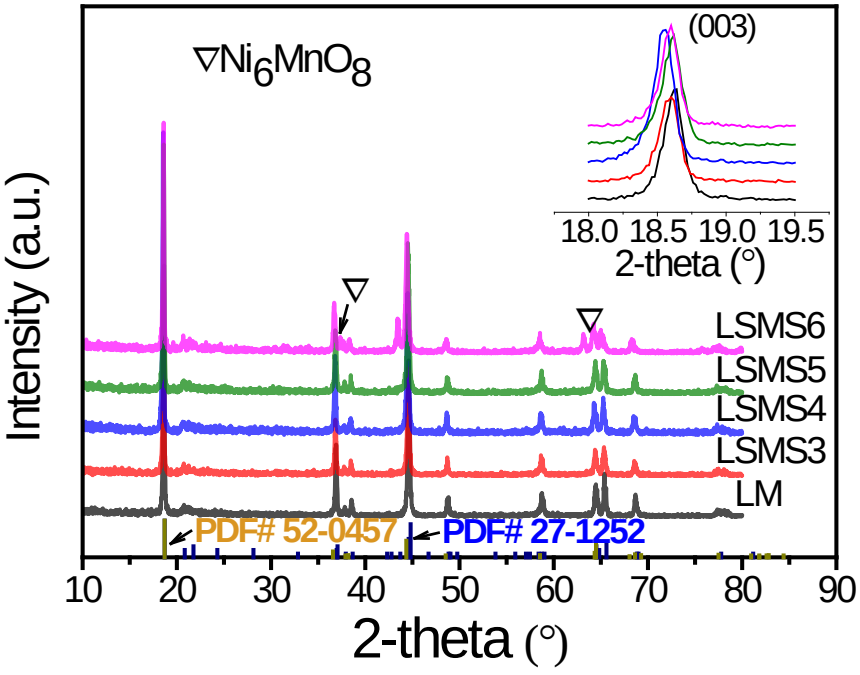

Figure S14. XRPD data of the LSM-coated LM at various coating temperatures.

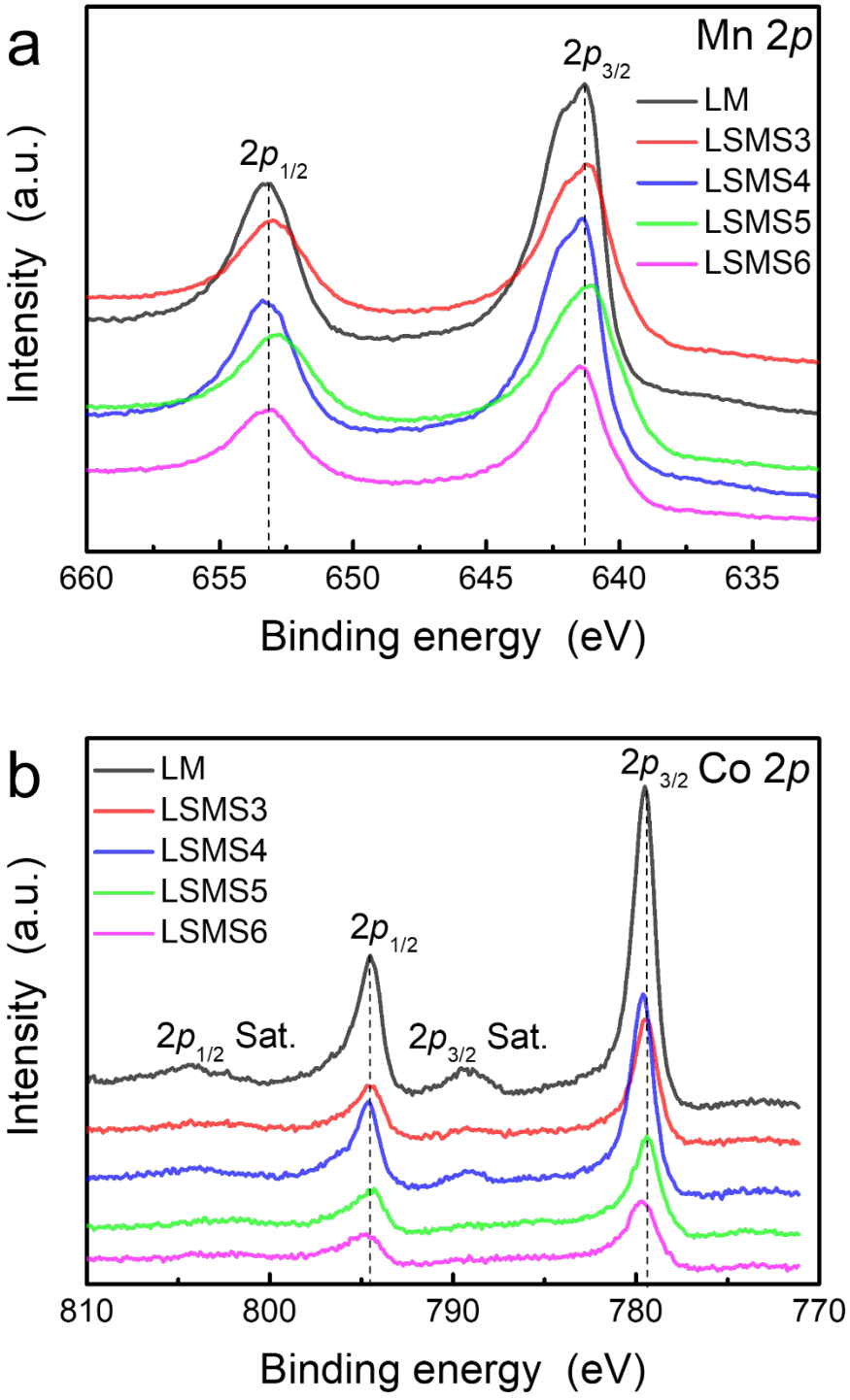
a
Mn 2p
2p3/2
2p1/2
LM
LSMS3
LSMS4
LSMS5
LSMS6
Intensity (a.u.)
660
655
650
645
640
635
Binding energy (eV)
b
LM
LSMS3
LSMS4
LSMS5
LSMS6
2p3/2 Co 2p
2p1/2
2p1/2 Sat.
2p3/2 Sat.
Intensity (a.u.)
810
800
790
780
770
Binding energy (eV)

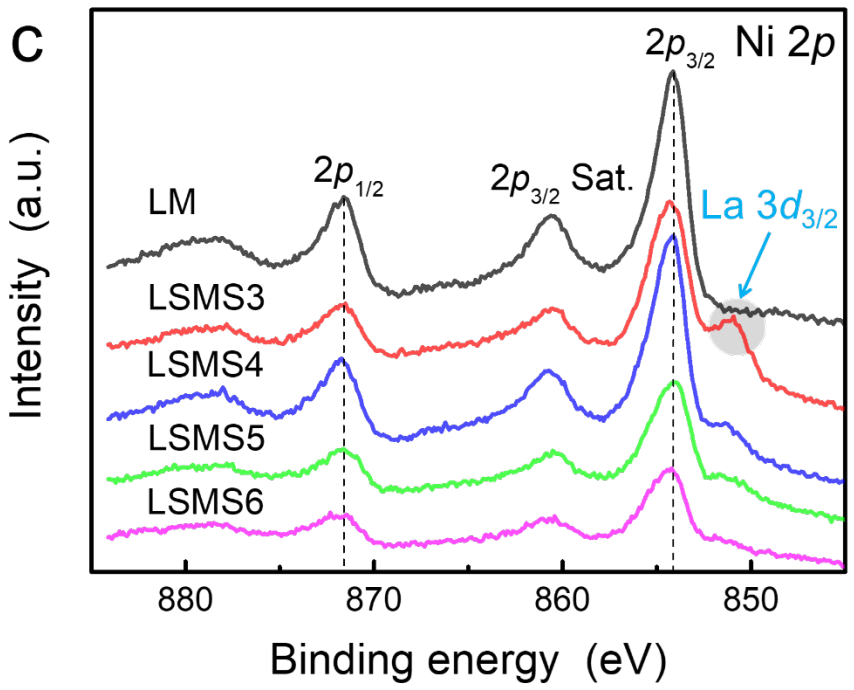

Figure S15. X-ray photoelectron spectra of pristine LM and surface modified LM synthesized at different temperatures. (a) Mn 2*p*, (b) Co 2*p*, (c) Ni 2*p*.

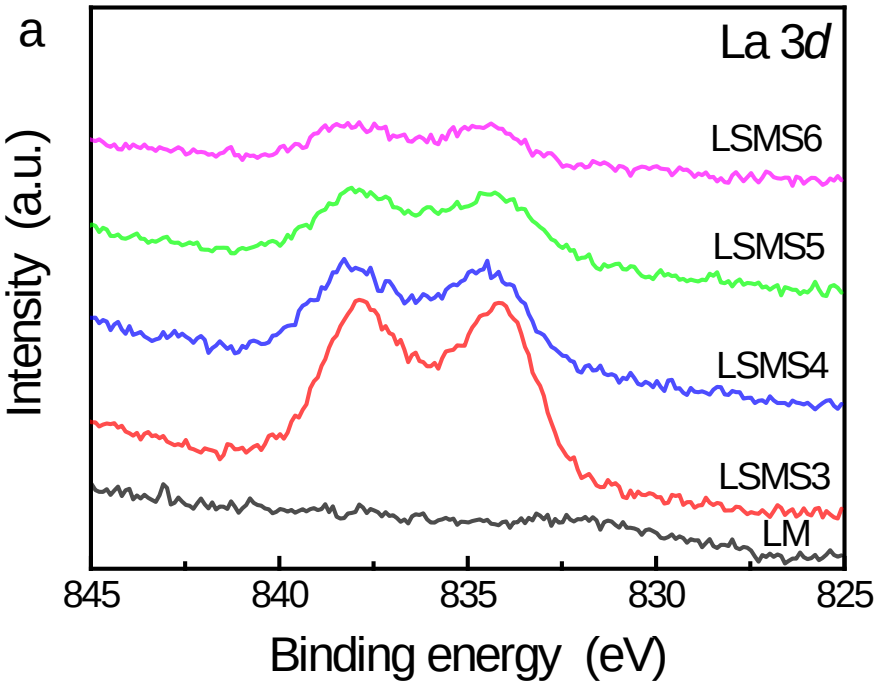

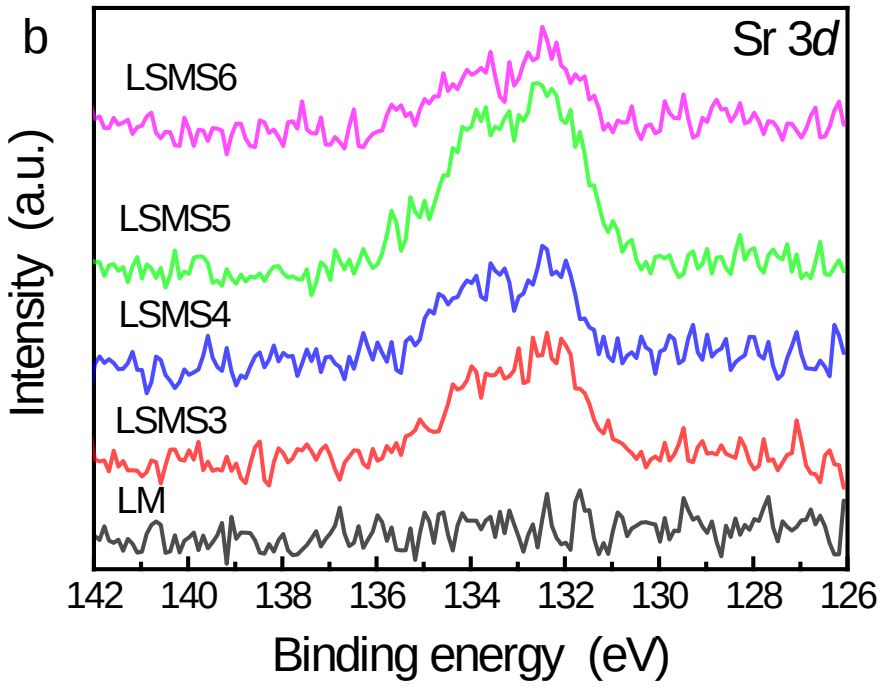

Figure S16. X-ray photoelectron spectra of pristine LM and surface modified LM synthesized at different temperatures (a) La 3*d* and (b) Sr 3*d*.

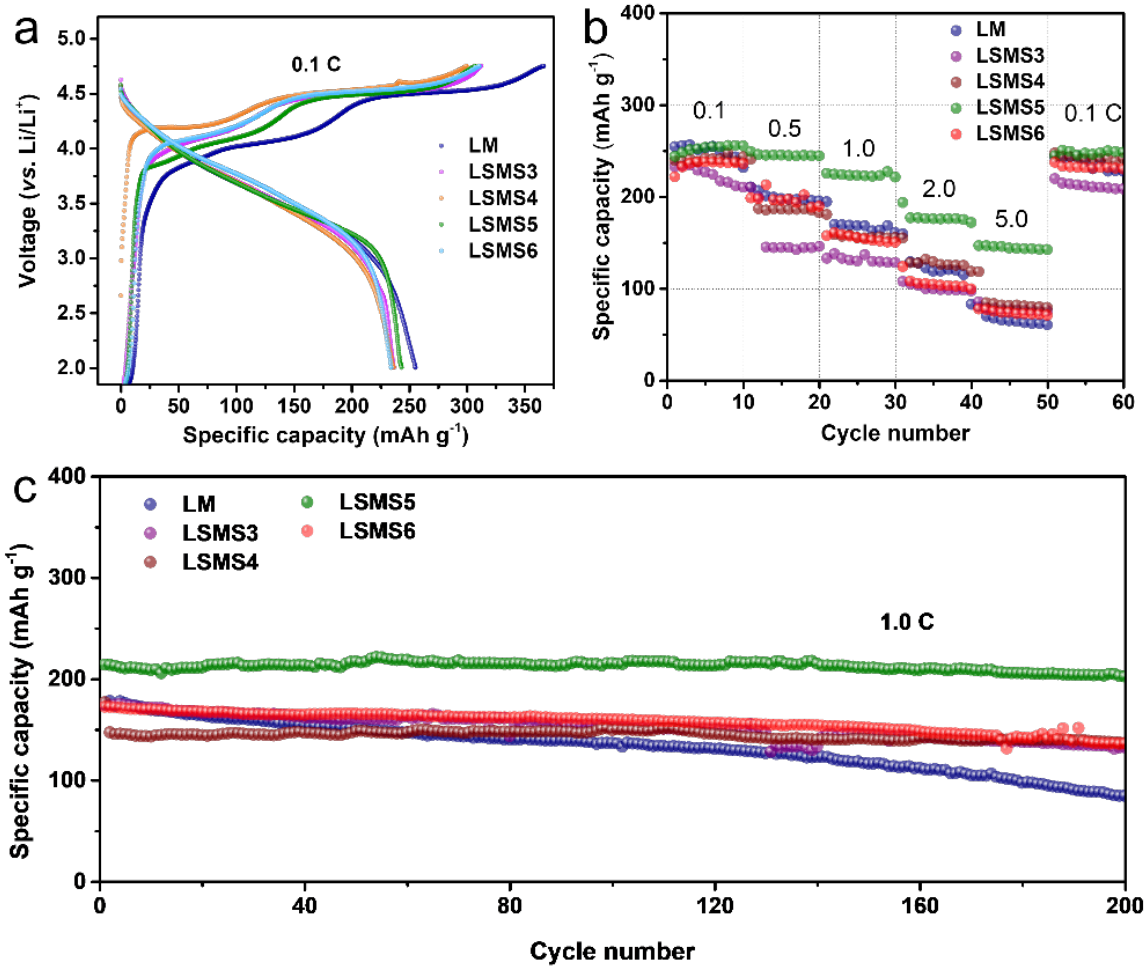

Figure S17. Electrochemical properties of pristine and LSM-coated LM synthesized at different temperature. (a) charge-discharge profile at 0.1 C; (b) rate capability, and (c) cycling performance at 1.0 C